UCLouvain

epl

École polytechnique de Louvain

Development of an inductive sensor for superparamagnetic nanoparticles detection and quantification

Author: **Nordin Trifiro**
Supervisor: **Jean-Pierre Raskin**
Readers: **Laurent Francis, Margo Hauwaert, Martin Lefebvre**
Academic year 2023–2024
Master [120] in Electrical Engineering

Acknowledgements

As with many works of this scale, this master thesis has been made possible only with the contribution of many people. Here is a non-exhaustive list of who offered advice, support, help, and proofreading throughout this year, but also tea, coffee, ping pong and much too long breaks.

I would first like to thank my supervisor, Jean-Pierre Raskin, for trusting me with this project. I would also like to give a very special thanks to Margo Hauwaert and Martin Lefebvre, for their constant support and their precious insights throughout this entire year.

Thank you to Laurent Francis, for accepting to take part in my jury and for his suggestion to explore the technique of frequency counting.

There are also many people who helped me with the technical side of things, so big shout out to Souley Djadjandi, Benoit Hubert, Pascal Simon and Simon De Jaeger.

Thank you to Brock, Ramy, and Justine for welcoming me in their office for the better part of a semester.

And finally, a big thanks to Laurence and Marion for proofreading my manuscript, even though they were drowning under the workload, and to all the people I forgot to mention but who supported me one way or another in the realization of this work. This is the conclusion of five amazing years, and I hope you will enjoy reading it as much as I enjoyed writing it (the interpretation of this sentence is left to the reader). With that being said, it is time to get serious, and I wish you a smooth and agreeable reading

Abstract

This research falls in line with the development of a point-of-care system for water quality monitoring by means of a paper-based sensor using the Later Flow Assay (LFA) technique. Specifically, this LFA employs superparamagnetic nanoparticles as label to detect bacteria in water. The main objective is to create a low-cost, portable system suitable for regions with significant water quality issues, but limited resources and equipment for monitoring.

The main focus of this work is the design of a magnetic sensor to detect and quantify nanoparticles at the LFA test line, with the constraint of using only off-the-shelf components to ensure affordability and portability. Two inductor-based solutions are explored.

The first solution is based on a design proposed in an article, that uses two pairs of primary-secondary coils. The primary inductors induce currents in their respective secondary coils, and the presence of nanoparticles is detected by measuring variations in the induced current. However, this method proved unsuitable in this context of this work, due to both sensitivity issues and complexity of implementation.

The second solution measures the frequency variation in the oscillation frequency of an LC-oscillator. The presence of nanoparticles in the inductor of the oscillator causes a shift in its inductance value, thereby altering the frequency at which the circuit oscillates. This approach yielded promising results, detecting down to 15 µg of nanoparticles on a sample, and displaying a linear relationship between the mass of nanoparticles and the amplitude of the frequency variation. Moreover, both the oscillator and the entire frequency-conditioning chain can be implemented with off-the-shelf components and a Teensy microcontroller. Several improvements were identified that could further lower the limit of detection reached in this initial iteration.

Introduction

Ensuring access to safe, drinkable water on a daily basis is essential to prevent the spread of diseases and infections. However, the regions where the access to clean water often lack the resources and equipment for an effective water quality monitoring. To address this issue, a point-of-care bacteria biosensor is being developed. To be used in this context, this sensor has to meet several constraints. It must be low-cost, portable, user-friendly for non-specialized personnel, and capable of providing rapid, robust, and sensitive detection.

The solution that is currently explored utilizes the Lateral Flow Assay (LFA) technique to detect the presence of bacteria in the water. The principle of operation of the LFA is illustrated in Figure 1.

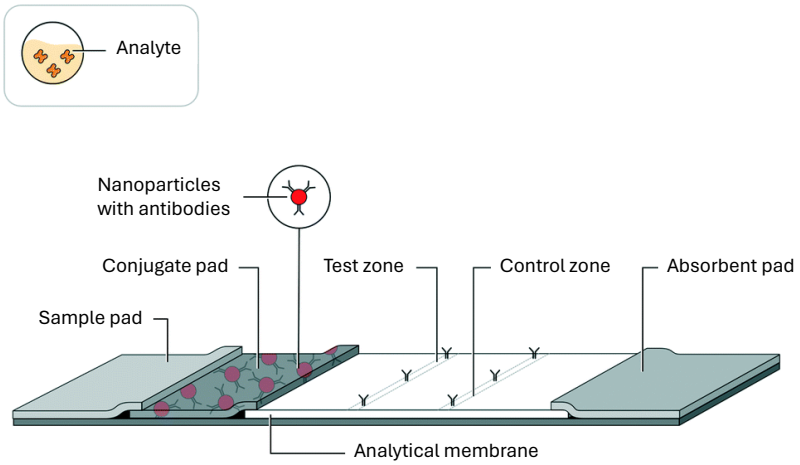

Figure 1: *Working principle of the LFA. The analyte is deposited on the sample pad and moves up the membrane by capillarity. When it reaches the conjugate pad, the targeted agent conjugates with functionalized nanoparticles. These nanoparticles are then brought by the target agent to the test and control lines, where they can be detected. Image from [1]*

The analyte with the targeted agent we want to detect is deposited on the sample pad of the test, and moves up the length of the membrane by capillarity. At the conjugate pad, the target agent binds with a labelled detection reagent, which is then brought to the test and control zones. The detection reagent is typically one or more different antibodies conjugated to a nanoparticle label. Depending on the type of label that is used, the actual detection can be colorimetric, non-colorimetric or magnetic [1]. LFA offers several advantages, including an analysis time of less than 30 minutes, ease of use, low cost, repeatability, and the absence of the need for specialized equipment [2].

This research focuses on a LFA with a paper-based analytical membrane, combined with superparamagnetic nanoparticles (MNP) as the detection reagent. The main benefit of

using MNP as reagent is that, contrary to colorimetric or non-colorimetric methods relying on optical detection, detection of MNP is carried out through a magnetic sensor. This approach allows for a quantitative detection, with a precise measurement of the concentration of the target agent, as opposed to the qualitative detection offered by other labelling method.

This work in particular focuses on the development of the magnetic sensor for detecting and quantifying the MNP in the LFA. Various methods exist to detect nanoparticles, with some capable of detecting the presence of a single bead [3]. However, for this magnetic sensor to be relevant in the context of this research, it must meet the specifications on cost, portability, and usability by non-specialized personnel. The decision was then made to develop a solution implementable with off-the-shelf components only, based on inductors. The use of off-the-shelf components ensures the portability and low-cost, and inductors are cheap and easy to make. Finally, a usual LFA test can contain from 0.1 to 50 µg of nanoparticles, which gives the operation range of the sensor.

The main objective of this work is to determine whether it is feasible to build a transducer sensitive enough to detect nanoparticles quantities in the µg range, using only off-the-shelf components. Two solution are explored in this thesis.

The first solution is based on a design proposed in an article, that uses two pairs of primary-secondary coils. The primary coils induce a current in their respective secondary coils, and the nanoparticles are detected by measuring variations in this induced current. However, this method proved unsuitable in this context of this work, due to both sensitivity issues and complexity of implementation.

The second solution measures the frequency variation in the oscillation frequency of an LC-oscillator. The presence of MNP in the inductor of the oscillator causes a shift in its inductance value, thereby altering the oscillation frequency of the oscillator. This solution offers the advantage that it can be fully implemented with off-the-shelf components, ensuring low-cost and portability. The measurement of this frequency can be performed with a simple microcontroller, which also makes it possible to develop an accessible user interface.

This thesis is organized in three main chapters. The first chapter provides a brief consists of a review of the main nanoparticles detection techniques that are used in LFA contexts. The second chapter focuses on the first solution that was explored, first by introducing the theoretical concepts involved, then by discussing an actual implementation. As this technique proved ineffective in this work, the third chapter develops the second technique that was explored. A theoretical background is given, then a practical implementation is presented and its performance regarding nanoparticles detection are discussed. Finally, perspectives are given for future works to improve the performance of the second system, along with a summary of the conclusions reached throughout this thesis.

Contents

Chapter 1

State of the art

1.1 Nanoparticles detection techniques

There exist multiple techniques to detect the presence of nanoparticles, each with their advantages and disadvantages. A review of the different techniques that can be used to detect nanoparticles, with their main advantages and disadvantages, can be found in [4] and [3]. However, in the context of Lateral Flow Assay, there are four techniques that are usually preferred [5]:

- Sensor based on the Giant Magnetoresistance effect (GMR)
- Frequency mixing
- Measurement of the resonant frequency of a coil
- Impedance measurement of a coil

While the first technique uses a magnetoresistive magnetometer, all the others are based on coils. The main advantage of using coils is their linearity and the fact that it is possible to detect magnetic signals in a broad range. The technique based on GMR is also able to measure fields in a relatively high range, although not as broad as with coils. Figure 1.1 compares the range of detection of various ways of measuring magnetic field, with both the search coil and the magnetoresistive magnetometer among the sensors with the highest range.

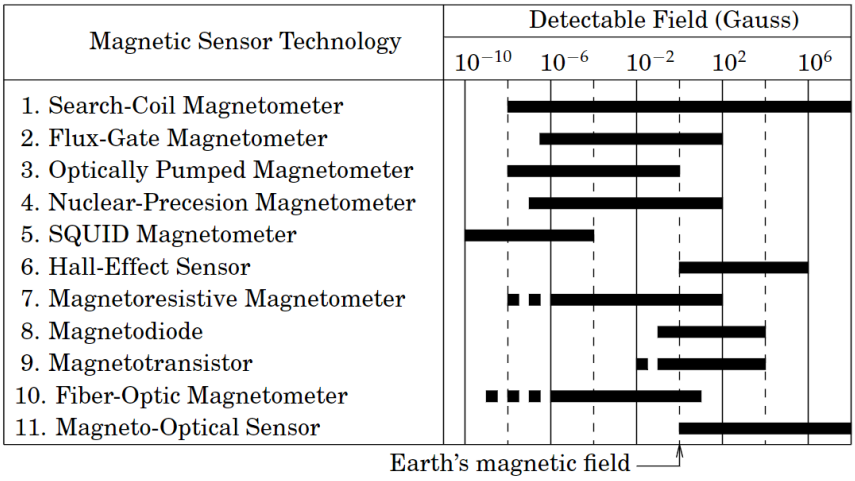

Figure 1.1: *Detection range of the different techniques used to measure a magnetic field. 1 G =* 10^{-4} *mT. Image taken from [6]*

1.1.1 Giant magneto resistance

The GMR effect is a change in the electrical resistance of a sensor, when an external field is applied. This sensor is composed of several thin ferromagnetic layers alternating with nonmagnetic layers in order to amplify the magnetoresitance effect. In the presence of an external magnetic field, the magnetization of the ferromagnetic layers relative to each other changes, causing a change in the resistivity of the sensor[7]. This effect was discovered in 1988 by Albert Fert and Peter Grünberg, discovery for which they received the 2007 Nobel Prize in Physics.
If the magnetization of the different layers is parallel, the resistance is lower than if the alignment is antiparallel. Figure 1.2 illustrates this concept for a two-layers sensor.
The magnitude of this effect can be defined as :

$$\frac{\Delta R}{R} = \frac{R_{\uparrow\downarrow} - R_{\uparrow\uparrow}}{R_{\uparrow\uparrow}}. \tag{1.1}$$

Here, $R_{\uparrow\downarrow}$ and $R_{\uparrow\uparrow}$ are, respectively, the resistivity for parallel and antiparallel alignment. This effect is caused by the fact that the transport of electrons in a magnetic metal depends on their spin. If a magnetic field is applied, it changes the direction of the electron spins and have an impact on the alignment of the layers' magnetization and hence the resistivity of the sensor.

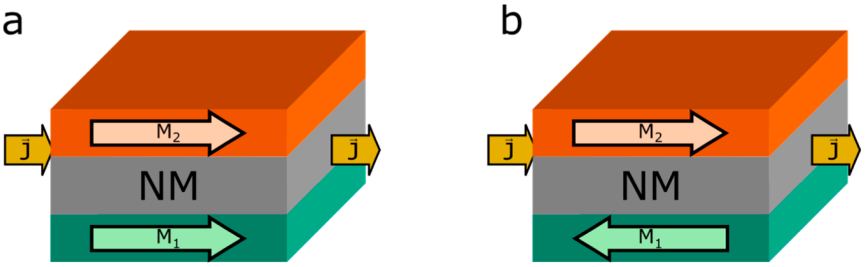

Figure 1.2: *GMR double layer in Current in Plane configuration. (a) Layer magnetization M_1 and M_2 parallel, the sensor resistivity is low ; (b) Layer magnetization M_1 and M_2 antiparallel relative to each other, the sensor resistivity is high. NM is the nonmagnetic layer and $\vec{J}$ the current density in the sensor. Image from [7]*

.

To detect nanoparticles using this technique, a biasing magnetic field is applied on the sensor, usually with coils or permanent magnets. The presence of nanoparticles introduces a perturbation in this biasing field, causing a change in the resistivity of the GMR sensor. As this is a resistive sensor, it can be interfaced using a Wheatstone bridge [8].

It is possible to increase the sensitivity of such sensor by using the spin-valve technique, which also uses the GMR effect, but the structure of the sensor is more complex, usually with two magnetic layers, and several other layers separating them. This structure fixes the magnetization of one of the magnetic layer (the pinned layer), while the magnetization of the other layer is let free. The detection is performed by measuring the angle between the magnetization of the two layers [9]. A single 500 nm nanoparticle was detected in [10] using a spin-valve sensor. The detection of 20 nanoparticles with a diameter as low as 16 nm was achieved in [9].

The design of the sensor itself has the biggest impact on the performance. Depending on its size, the number of layers, and the type of layer used, the magnitude of the GMR effect can vary [11]. The main disadvantage of this technique compared to the others is that it requires microfabrication.

1.1.2 Frequency mixing

This technique is based on the Brownian and Neel relaxation properties of nanoparticles and their non-linear magnetic response when excited in a certain way. The nanoparticles are excited with two signals, one with low frequency f_1 and high amplitude, and another with high frequency f_2 and low amplitude. The low signal periodically brings the nanoparticles in and out of their magnetic saturation region. When MNP are not in saturation, they can be further magnetized by the second signal at a higher frequency, which then contributes to the resulting induction signal [12], [13].

The response signal $U(t)$ is non-linearly modulated by both the high and the low frequencies and is measured at some frequency $f_i = mf_1 + nf_2$ with $m, n \in \mathbb{Z}$. The response at this combinatorial frequency is proportional to the quantity of non-linear magnetic material, or the number of magnetic beads (MB)[14]. The advantage of this technique is that nanoparticles of different size induce a different frequency response f_i. This means that such technique can be used to measure the distribution of nanoparticle sizes in a sample [12]. Figure 1.3 illustrates the working principle of frequency mixing.

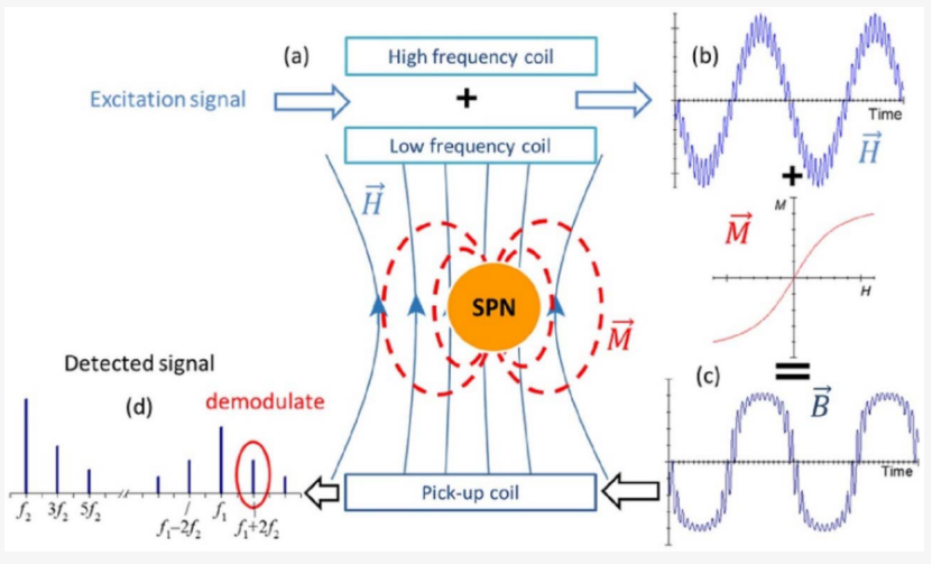

Figure 1.3: *(a) Setup of the application of the frequency mixing technique; (b) magnetic excitation field; (c) resulting magnetic flux density; (d) Fourier transform of the detected signal. The frequency component f_i selected for the detection if circled in red. $\vec{M}$ is the magnetization direction of the MNP, $\vec{H}$ and $\vec{B}$ the excitation and the resulting magnetic field, respectively. Image from [15]*

The two excitation signals can be generated using excitation coils, and the resulting signal can be detected with a pickup coil. It requires however powerful equipment, such as lock-in amplifiers, to precisely measure the frequency response of the system.

The main parameters that influence the detection are the nanoparticle size, the amplitude of the drive magnetic field, and the choice of m and n for the frequency f_i at which the frequency response is measured. Amounts as low as 0.4 ng of MNP, for a diameter greater than 16 nm can be detected with this technique [16], [12].

1.1.3 Measurement of the resonant frequency of an inductor

This is probably one of the most straightforward techniques to detect the presence of MNPs. The idea is to build a RLC circuit that has a resonant frequency ω_0,

$$\omega_0 = \frac{1}{\sqrt{LC}}. \tag{1.2}$$

This RLC circuit can be explicitly built with an inductor and a capacitor, or one can just use the intrinsic resonant frequency of a real inductor[17]. Indeed, every coil can be represented as shown in Figure 1.4, and has its own resonant frequency which depends on its inductance and parasitic capacitance value.

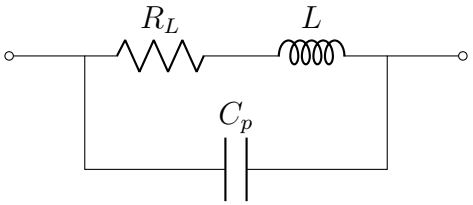

Figure 1.4: *Model of an inductor with the parasitic series resistance R_L and the parasitic capacitor C_p*

By putting MNP inside the inductor core, this changes the magnetic permeability of the core environment and thus the value of the inductance. This causes a shift in the resonant frequency of the circuit that can be detected in various ways, some more complicated than others.

A simple way to detect this shift is to use a Phase Lock Loop (PLL) controlling a Voltage Controlled Oscillator (VCO) where the oscillator is a LC-oscillator [18]. If the oscillation frequency of the VCO is changed due to the presence of nanoparticles, the control voltage generated by the PLL also changes in order to compensate for this variation. By measuring this voltage, one can determine whether nanoparticles have been detected.

1.1.4 Impedance measurement

This last technique is also based on detecting a change in the inductance value of an inductor. The impedance Z_L of a coil is given by

$$Z_L = j\omega L, \tag{1.3}$$

with L the inductance value of the coil, and $\omega = 2\pi f$ the pulsation in radian per second. As the nanoparticles provoke a change in the value of the inductance, they also impact the impedance of the coil. With appropriate equipment, this impedance can be extracted, giving an idea of the quantity of nanoparticles detected.
Even though the working principle of this technique is straightforward, it does require to have some equipment, such an Impedance Analyzer or a Vector Network Analyzer, able to accurately measure the value of the impedance of the coil. To reach the desired level of precision, such equipment is usually expensive, and only available in laboratories.

1.1.5 Summary of the techniques

Phys. quantity	Transductor	Meas. technique	LoD	Range	Ref.
Brown and Neel relaxation time	2 excitation coils - 1 pick up coil	Frequency mixing	0.4 ng	7 orders	[16]
			3 ng	3 ng - 70 µg	[14]
			0.12 µg/ml	0.12-1300 µg/ml	[19]
Giant magnetoresistance effect	GMR/GMI	Wheatstone bridge	64 ng	NA	[20]
			1.2 µg	NA	[21]
			0.84 µg	NA	[22]
Coil self-inductance variation	Single coil	Frequency var. meas.	10 μg	NA	[17]
			1.2 µg	1.2 - 40 µg	[18]
		Impedance meas.	$\approx 1\mu g$	NA	[23]
			$\approx 1\mu g$	NA	[23]

Table 1.1: *Summary of the commonly used nanoparticles detection techniques in the context of LFA. Regarding the range for each application, "NA" value denotes the fact that the range was not discussed in the article.*

Among these possibilities for the detection of nanoparticles, the choice has been made to work with coils and to focus on measuring the inductance variation induced by a change in the magnetic permeability of the core in presence of nanoparticles. Several reasons motivate this choice.

First of all, it has been shown in [24] that the impedance variation of an inductive sensor is linear. The sensor used in their article was composed of a copper track 120 µm wide and 35 µm thick. Their setup is shown in Figure 1.5, along with a graph displaying the relationship between the mass of nanoparticles and the impedance of the inductive sensor.

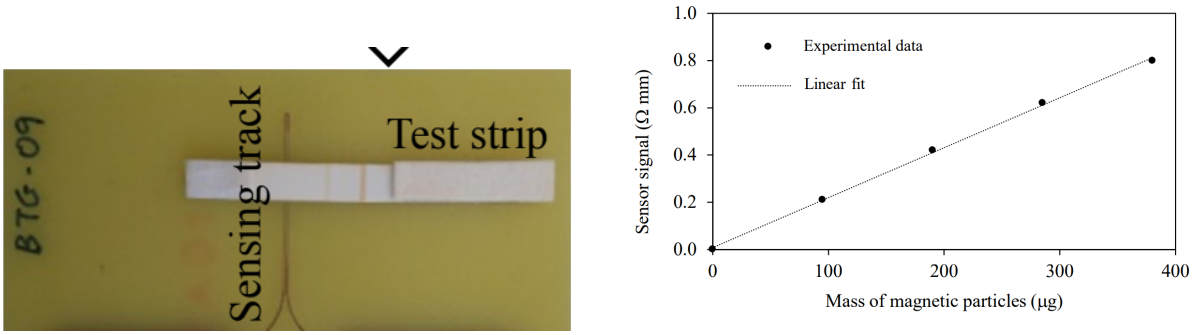

(a) *Inductive sensor used in [24]*

(b) *Impedance of the inductive sensor from [24] with respect to the mass of nanoparticles*

Figure 1.5: *Inductive sensor (left) and its impedance response with respect to the mass of nanoparticles (right)*

A linear impedance variation of the inductor implies a linear variation of the inductance since these two quantities are linearly related through the frequency of the excitation signal, as expressed by Equation 1.1.4.

Secondly, as expressed in Table 1.1 presented at the beginning of the chapter, search-coil magnetometer displays the widest range of detection. Having a broad range means that we are certain that we are not be limited by the saturation of the sensor itself.

Finally, a system based on coils is also the most likely to meet the cost requirement for the system we aim to develop. Indeed, some of the techniques to interface inductive sensors do not require any expensive equipment and can be designed with off-the-shelf components. The fabrication of the inductor itself is not complicated either and can be done by hand, by wounding wire around a support.

Chapter 2

Differential system using the induction principle to detect nanoparticles

The first method that was tried in this work to detect nanoparticles is the measurement of variations in the voltage induced by an excitation coil in a sensing coil. These variations are caused by two phenomenons.

Firstly, introducing nanoparticles in a coil changes the magnetic permeability of its core. As the inductance value of a coil depends on the magnetic permeability of its core, the nanoparticles thus also change the self-inductance value of the inductor in which they are introduced.

Secondly, in a system with an excitation coil inducing a voltage in a sensing coil, introducing nanoparticles in the system impacts the way the two inductors are coupled together. This effect, coupled with the change in the self-inductance of coils when the magnetic permeability of their core are modified, causes variations in the voltage induced by the excitation coil in the sensing coil. The first method that is discussed focuses on measuring these changes to detect the presence of nanoparticles in the system.

In this chapter, a quick review of the basic principles needed to understand this first solution is given. A system proposed in an article from 2005 by Jarkko Makiranta and Jukka Lekkala [25], in which a differential system with two pairs of excitation-sensing coils was simulated and theorized to detect tiny amounts of nanoparticles, is then discussed. Finally, the issues that arise when trying to detect nanoparticles by measuring variations in the voltage induced in a coil are presented.

2.1 Theoretical background

2.1.1 Principle of induction

The induction principle was first theorized by Michael Faraday and Heinrich Lenz in the 1830s, who derived what is known as the Lenz-Faraday law. This law quantifies the electromotive force ϵ induced in a loop when a variable magnetic flux Φ passes through it

$$\epsilon = -\frac{d\Phi}{dt}, \tag{2.1}$$

with the magnetic flux defined as

$$\Phi = \iint_S B \cdot dS \tag{2.2}$$

where S is the area through which the flux is calculated. Conversely, a current passing through a wire loop produces a magnetic field through and around the loop.

Mutual induction

From a circuit perspective, an alternative current passing through an inductor generates an alternative magnetic field B in the coil and around. If a second coil is placed close enough to the first one, such that a part of the alternative magnetic field generated by the first coil passes through the second one, an electromotive force is induced in the latter. If a current can circulate through the second coil, this induction phenomenon creates a voltage difference across the second inductor. This concept is illustrated in Figure 2.1.

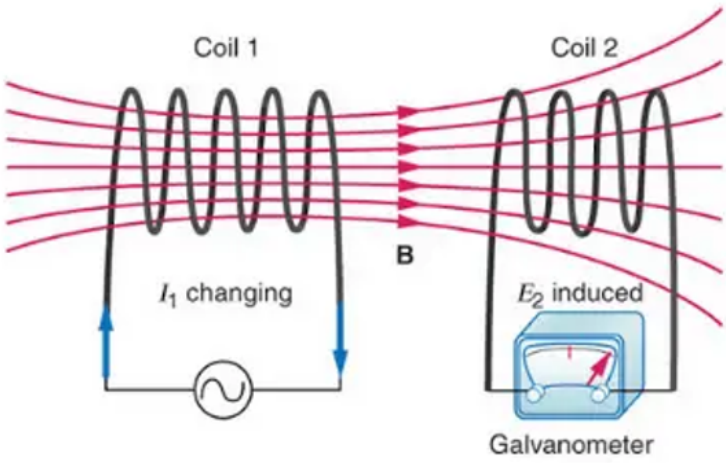

Figure 2.1: *Illustration of the induction phenomenon. The coil 1 generates a variable magnetic field B, which induces an electromotive force E_2 in the second coil. Image from [26]*

Reciprocally, the current induced in the second inductor also generates a magnetic field of its own, influencing the magnetic field in the first one. This mutual influence is known as the **mutual inductance** and is denoted M.

The mutual inductance between two coils depends on several factors, namely the geometry of each individual coil, and their relative position with each other [27]. Let us define N_1 and N_2 the number of wire loops in each inductor 1 and 2, Φ_{21} and Φ_{12} the flux generated by the first coil (resp. the second) and intercepted by the second (resp. the first),

and I_1 and I_2 the currents flowing in the two inductors respectively. The mutual inductance M_{21} of coil two with respect to coil one can then be expressed as

$$M_{21} = \frac{N_2 \Phi_{21}}{I_1}, \tag{2.3}$$

and the mutual inductance M_{12} of coil one with respect to coil two is

$$M_{12} = \frac{N_1 \Phi_{12}}{I_2}. \tag{2.4}$$

Also, $M_{12} = M_{21} = M$, and it can be either positive or negative depending on the way the two coils influence each other. If the magnetic field of each coil is in the same direction, the influence is positive. Conversely, if the magnetic fields are in opposite directions, the two fields have a negative influence on each other.

Figure 2.2 shows a simple circuit where each coil is modelled with an ideal inductor in series with a parasitic resistor and in parallel with a parasitic capacitor. The inductor L_p in the primary circuit is excited with an alternative signal V_{in}, and is coupled with the inductor L_s in the secondary circuit through the mutual inductance M.

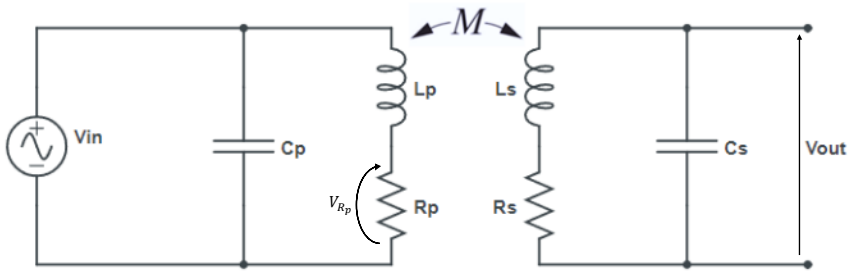

Figure 2.2: *Induction phenomenon from a circuit perspective : equivalent circuit*

Coupling factor

The coupling factor k is a metric denoting how strongly the coupling between two inductors is. It is defined from the mutual inductance M between the two coils and their respective inductance L_1 and L_2,

$$k = \frac{|M|}{\sqrt{L_1 L_2}}. \tag{2.5}$$

The greater the mutual inductance with respect to the self-inductance of the coils is, the greater the coupling factor is. The maximum value it can take is 1, denoting a perfect coupling between the two inductors. This also implies that the maximum value for the mutual inductance is

$$M = \sqrt{L_1 L_2}. \tag{2.6}$$

Conversely, a coupling factor of zero indicates that there is no coupling between the two inductors, hence no mutual induction.

Induced voltage

The value of the electromotive force ϵ induced in the secondary coil depends on the magnetic field intercepted by this coil. It is possible to express the electromotive force in the frequency domain as a function of the current passing through the primary inductor and the mutual inductance. Using phasor notation, this gives

$$\epsilon = -j\omega B_p S_{eq} \tag{2.7}$$
$$= -j\omega M I_{L_p}, \tag{2.8}$$

with $B_p S_{eq}$ being the magnetic flux generated by the primary coil and intercepted by the second, M the mutual inductance between the inductors, and I_{L_p} the current flowing through the primary coil. To obtain this expression, the integration surface was reduced to the equivalent surface S_{eq} on which B_p is constant. As the presence of nanoparticles impacts the value of the mutual inductance, their influence is directly translated into a variation in the induced voltage.

The circuit 2.2 was simulated on LTSpice, and the evolution of the voltage across the resistor R_p and of the output voltage is shown in Figure 2.3.

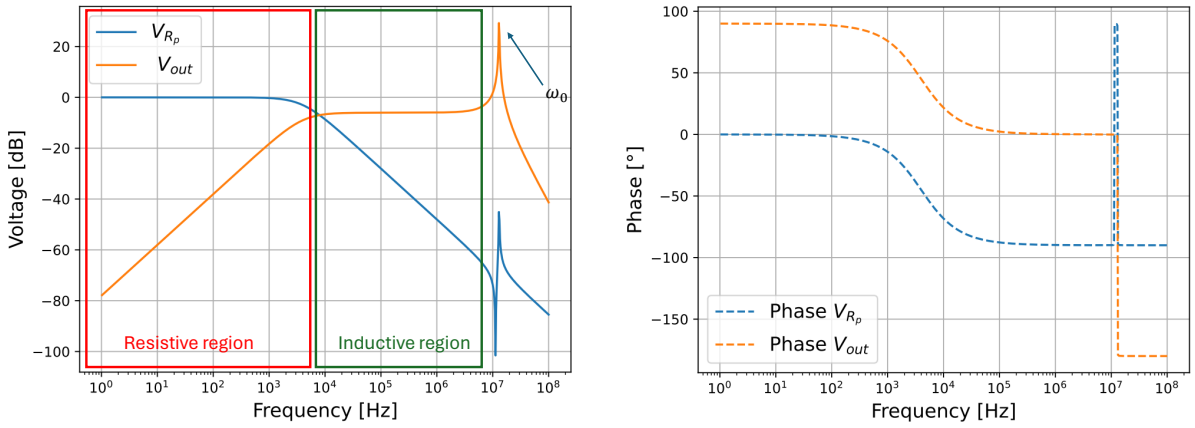

Figure 2.3: *LTSpice simulation of the evolution of the voltage across the resistor R_p from Figure 2.2and the output voltage V_{out}. $L_p = L_s = 20\mu H$, $C_p = C_s = 10pF$, $R_p = R_s = 0.5\Omega$. The amplitude of the voltage is represented on the left, while its phase is represented on the right. The peak at ω_0 corresponds to the resonance frequency of the circuit (which is the same for the primary and the secondary as the components are the same in each circuit.*

The current I_{L_p} can be expressed as

$$I_{L_p} = \frac{V_{in}}{R_p + j\omega L_p} \tag{2.9}$$

At low frequency, the series resistance R_p dominates over the impedance of the inductor $j\omega L_p$, and the behavior of the primary circuit is mostly resistive. This region is framed in red in Figure 2.3. The magnetic field generated by the primary coil is small, and hence the induced voltage is small.

As the frequency increases, the impedance of the inductor increases, until its magnitude is equal to the series resistance R_p. At this point, the inductive impedance becomes dominant, and the behavior of the primary circuit is mainly inductive. The magnetic field generated in

the secondary remains constant with respect to the frequency. When the circuit operates in the inductive region, the series resistance can be neglected in the expression of the current flowing in the primary circuit, giving

$$I_{L_p} = \frac{V_{in}}{j\omega L} \tag{2.10}$$

This expression can be injected in the expression of the electromotive force, leading to

$$\epsilon = -\frac{MV_{in}}{L} \tag{2.11}$$

As expressed by this relation, in the inductive region the magnitude of the electromotive force does not depend on the frequency. And as it is purely real, its phase is 0°.

Finally, at frequencies higher than the resonance frequency, the influence of the parasitic capacitance C_s starts to impact the output voltage, first by creating a peak in amplitude at the resonant frequency

$$\omega = \frac{1}{\sqrt{L_s C_s}} \tag{2.12}$$

Then by creating a small signal short circuit to the ground as its impedance decreases with frequency, causing the output voltage to drop.

In the context of nanoparticle detection by measuring a change in the amplitude of the induced voltage in a coil, the system has to work in the inductive region framed in green in Figure 2.3, where the induced voltage is constant with respect to the frequency. This ensures that variations in the induced voltage are not due to variations in the frequency of the excitation signal but are caused by nanoparticles.

2.2 Detecting nanoparticles using induction in a differential system

2.2.1 General idea and context

In 2005, Jarkko Mäkiranta and Jukka Lekkala published the paper [25] "*Modeling and Simulation of Magnetic Nanoparticle Sensor*" in which they describe a way to detect nanoparticles using differential detection. Their idea is to have a system composed of two identical pairs of primary-secondary coils. The primary coils are connected in series and induce a current in their respective secondary coil when excited by an alternative signal. Meanwhile, the two secondary coil are reversed-coupled in series, i.e., they are connected in such a way that the current I_1 induced in the first coil has an opposite direction to that of the current I_2 induced in the second coil. At equilibrium, the coupling factor of both pairs of primary-secondary coils is equal, I_1 and I_2 are then equal in magnitude, but have opposite direction, and they perfectly cancel each other. This configuration is shown in Figure 2.4, where the excitation circuit is in blue, and the sensing circuit is in green.

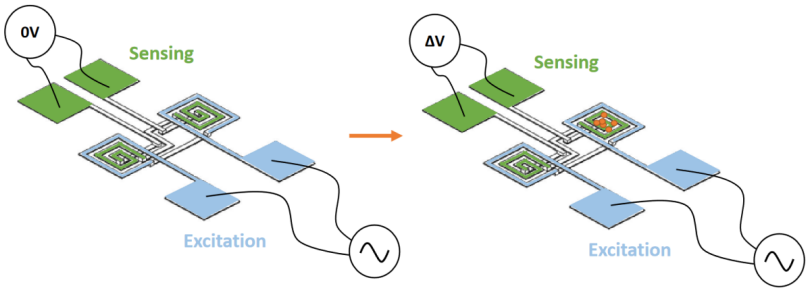

Figure 2.4: *System proposed by [25]. The excitation coils are in blue, and the sensing coil in green. On the left, the circuit is perfectly balanced and the output voltage of the secondary circuit is zero. On the right, nanoparticles on one of the sensing coil introduces an imbalance, which creates a non-zero output voltage.*

At equilibrium and in absence of nanoparticles, the system should be perfectly balanced, and the voltage difference across the sensing coils should be zero. When nanoparticles are deposited on one of the pair, it changes the magnetic permeability of the core of the inductors on which they have been deposited. This introduces an imbalance in the system as it changes the coupling factor between the inductors of the pair. The magnitude of the induced current in the sensing coil changes too, which translates in a measurable non-zero voltage difference across the two sensing coils

The results presented in the article are encouraging, as shown in Figure 2.5 where a single nanoparticle with a diameter of 250 nm caused an imbalance generating a current of 425 nA. For 1000 MNP, this induced current was around 0.4 mA.

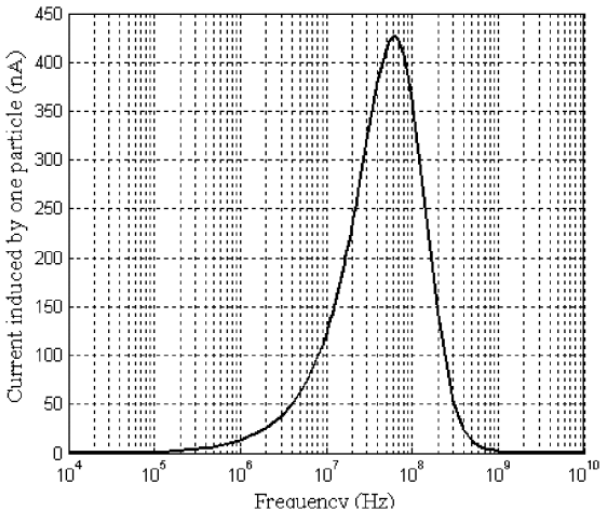

Figure 2.5: *Simulated induced current caused by the presence of one nanoparticle on one of the sensing coil, in the configuration of Figure 2.4[25].*

However, although this solution is very elegant on paper, the article only presents simulation results, without any experimental validation. The first part of this work is then to determine whether this solution is viable and could offer the predicted performances with all the non-idealities of a physical implementation. Especially as one of the biggest difference between the design that is simulated in the article and our design would be the size of the coils. Indeed, theirs are at the micrometer scale, while ours are at the centimeter scale, as the necessity to develop a low-cost solution precludes the use of microfabrication.

2.2.2 Differential and absolute detection

One of the first questions we sought to answer was whether the differential system presented hereabove was really advantageous compared to a system with a single pair of inductors. In such system, we would only measure the absolute value of the induced voltage, and depending on its value, we could determine whether nanoparticles were introduced in the sensing coil.

The biggest advantage a differential system has over the one with a single coil is that it is very efficient to remove environmental noise, i.e. noise caused by external sources such as temperature variation, supply voltage variation, etc. The reason for that is since the inductors are relatively close to each other and connected to the same circuit, they are affected in the same way by these variations. Because of the way the coils are connected in such a system, these variations are subtracted. Such a feature is crucial in our case, as in order to detect small quantities of nanoparticles (15 µg and less), the system has to be very robust regarding noise variations. Measurements (see Section 3.4.2) show that for amounts smaller than 100µg, one can expect a change of less than 0.05% in the self-inductance of a coil of a few µH. Naturally, the inductors that were measured in section 3.4.2 are not designed for a differential detection, and in a system based on voltage induction, there is the coupling factor variation in addition to a change in the self-inductance of the coils. Nevertheless, this gives an order of magnitude for amplitude of the variations this system needs to be able to detect, if we are to work with inductors with an inductance value between 10 and 30 µH.

As the induced voltage depends linearly on the mutual inductance value, if we consider an induced voltage of 1V, a variation of 0.05% of M means that the interface must be able to discriminate a 0.5mV variation of the output voltage.

Figure 2.8a shows a simulation of the differential system, where the inductors are all perfectly identical, and an imbalance of 0.1% in the coupling factor was introduced between the two pairs of coils. The resulting output voltage is at -68 dB in the inductive region, which corresponds to a magnitude of 0.3 mV.

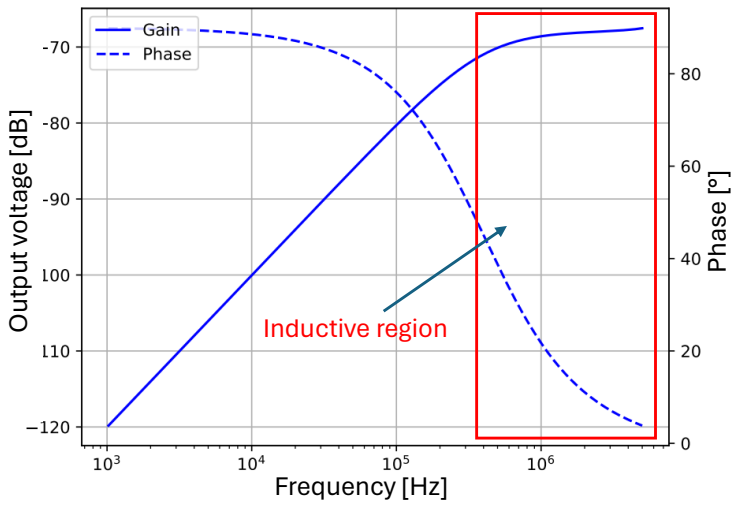

Figure 2.6: *LTSpice simulation of the output voltage caused by an imbalance of 0.1% of the coupling factor between the two pair of exciting/sensing coils of the differential system. The four inductors of the system have the same parameters :* $L = 10\mu H$, $R_s = 0.2\Omega$, $C_p = 10pF$

As exposed in this section, the voltage variations are really tiny, the system thus needs to be very robust to noise. To this end, the differential system has a big advantage over the absolute system with a single pair of coils, as it removes external noise by design.

2.3 Measurements results

The differential system described in the article was built with coils wound around a 3D-printed support. Figure 2.7 shows the inductors that were used to test this technique.

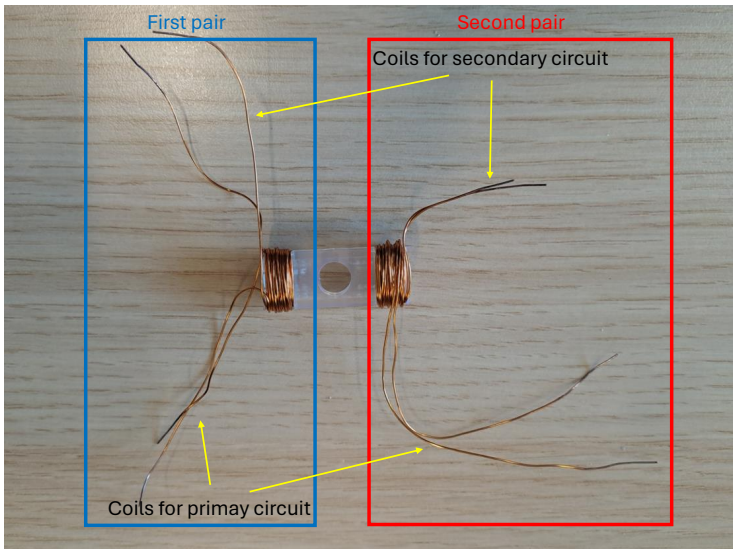

Figure 2.7: *Differential system that was built to test whether such technique was viable for the targeted application*

The coils of the primary circuit of the first and second pair were connected in series and excited with a sinusoidal signal with an amplitude of 500 mV and a frequency ranging from 1 kHz to 1 MHz. The coils in the secondary were reverse-coupled in series. Both the generation of the excitation signal for the primary circuit and the measurement of the output signal of the secondary circuit was done with the MFLI Lock-in amplifier from Zurich Instrument. Three measurements were performed, the first one without any nanoparticles, the second one with a sample containing 1 mg of nanoparticles inserted in one of the pair of coils, and a third one with a sample containing 25 µg of nanoparticles inserted in one of the pair of coils. The results are shown in Figures 2.8a and 2.8b show the measured voltage at the output of the secondary circuit, and the voltage difference between the voltage with and without nanoparticles, respectively.

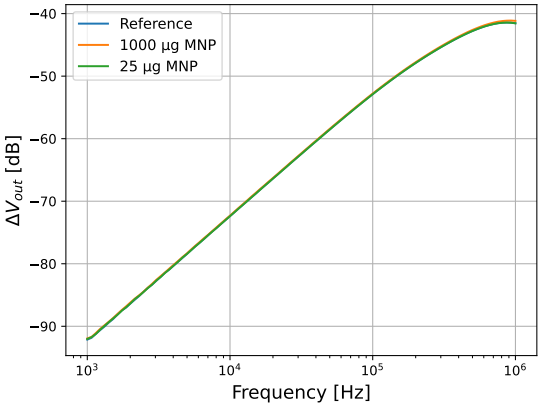

(a) *Measured voltage at the output of the secondary circuit of the differential system, without nanoparticles, with 1 mg and with 25 µg.*

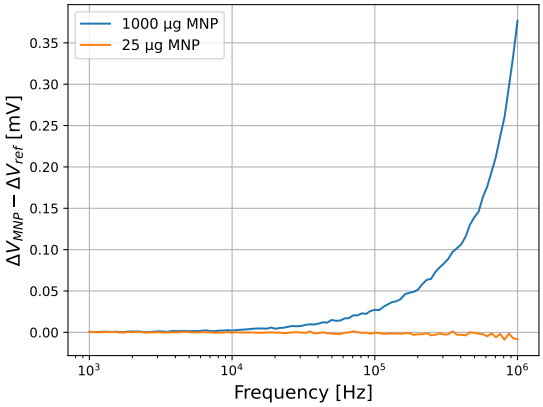

(b) *ΔV between the output voltage with nanoparticles V_{MNP} and the voltage without nanoparticles V_{ref}, for 25 µg and 1 mg of nanoparticles*

As can be seen in Figure 2.8b, the output voltage variation caused by the nanoparticles compared to the output voltage without nanoparticles is around 350 µV at 1 MHz for the sample containing 1 mg of MNP. The sample containing 25 µg of nanoparticles did not even produce a detectable ΔV with the reference voltage. This clearly shows that this technique, when using inductors with sizes of a few millimeters to a few centimeter, is not suitable. The constraint on the size of the inductors comes from the fact that, in order to keep the cost of the sensor low, we want to implement this system using off-the-shelf components. Using inductors whose size is smaller than 1 mm would require microfabrication, which is then non-desirable.

2.4 Issues with differential detection

As presented in the previous section, the differential detection in the context of this work is not suitable, for several reasons.

Size of the inductors

The influence of the nanoparticles on the coupling between two coils is caused by a change in the magnetic permeability of their core. To this end, the greater the volume of the core occupied by the nanoparticles, relative to the total volume of the core, the greater the change in permeability is.

In the article on which this discussion is based, the inductors used were planar square planar coils with a diameter of around 100 μm, which is already a big difference compared to the inductors that would be used in our system. Their inductance can be estimated using [28] :

$$L = \frac{\mu N^2 d_{avg} K_1}{2}\left[\ln\frac{K_2}{\rho_r} + K_3\rho_r + K_4\rho_r^2\right], \tag{2.13}$$

where μ is the magnetic permeability of the core, and N the number of turns. The coefficient K_i are the fitting parameters whose values for planar inductors can be found in [28]. d_{avg} and ρ_r are the average diameter and the fill ratio, respectively. They can be calculated as

follows, with d_{out} and d_{in} defined in Figure 2.9

$$d_{avg} = \frac{d_{out} + d_{in}}{2} \tag{2.14}$$

$$\rho_r \frac{d_{out} - d_{in}}{d_{out} + d_{in}} \tag{2.15}$$

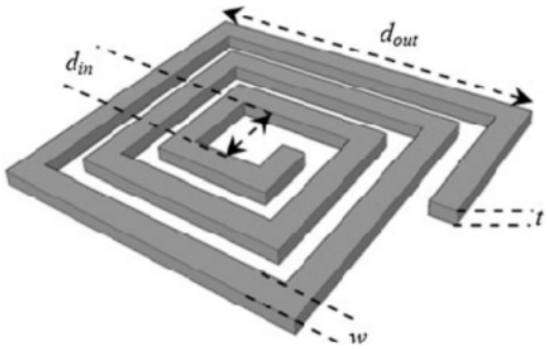

Figure 2.9: *Planar inductor - parameters definition [29]*

Using this formula for planar inductor, the value of the inductors used in the article on which this discussion is based can be estimated to be less than a nH. Using such inductors would require microfabrication, thereby increasing substantially the cost of the entire system.

Frequency of operation

As demonstrated in the theoretical background, inductors must be in their inductive region of operation to ensure that the induced voltage is maximum, and also that a variation in the output voltage is caused by MNP and not a frequency variation of the excitation signal. This might require the system to work at high frequencies, in the MHz range, as the size of the inductor - and therefore its inductance - needs to be reduced. In the article, the maximum induced current in the sensing coil was observed at an excitation frequency of 67.5MHz. Generating such high frequencies on a Printed Circuit Board (PCB) is not trivial and might also increase the cost of design and fabrication. Moreover, higher frequencies goes hands-in-hands with higher power consumption, particularly as the parasitic capacitances in the circuit switch more often.

Excitation signal generation and interfacing

Regarding the excitation circuit, the inductive behavior starts to take the upper hand over the resistive when the magnitude of the impedance of the inductor is equal to the series resistance, that is

$$|j\omega L_p| = R_p. \tag{2.16}$$

The greater the series resistance, the higher the frequency of the excitation signal needs to be to reach the inductive region. The series resistance then has to be minimized in the primary, but this comes at the cost of power consumption. In the article, they excited the primary coils with a current of 1A in the simulation. Not only does it increase substantially the power consumption, but it also demands powerful drivers to be able to provide that amount of current. It is already difficult to generate that type of signal in a laboratory, with

adapted equipment, it is then even more difficult to do it on a portable PCB.

Furthermore, interfacing the secondary circuit to be able to detect very small changes in the output voltage is not trivial either. There exist multiple techniques to detect tiny voltage variations, such as a lock-in detection, for example. However, most of them are not suitable for simple low-cost implementation on PCB, as they require complicated electronics or expensive instruments.

2.5 Conclusion

As exposed in this chapter, using the induction principle to build a differential system appears at first to be a very simple and elegant solution for detecting and quantifying nanoparticles. However, in the context of this work, where the aim is to develop a portable, low-cost solution to this problem, there seem to be too many challenges to overcome when trying to develop an actual prototype.

Nevertheless, the simulation does suggest that such a system could detect very small amount of nanoparticles. Figure 2.10 from [25] shows the magnitude of the current flowing in the sensing coils due to the imbalance introduced by MNP, simulated at a frequency of 67.5 MHz. The simulation indicates that a single 250 nm nanoparticle should produce a current of 425 nA, and a thousand particles generate a signal up to 0.4 mA.

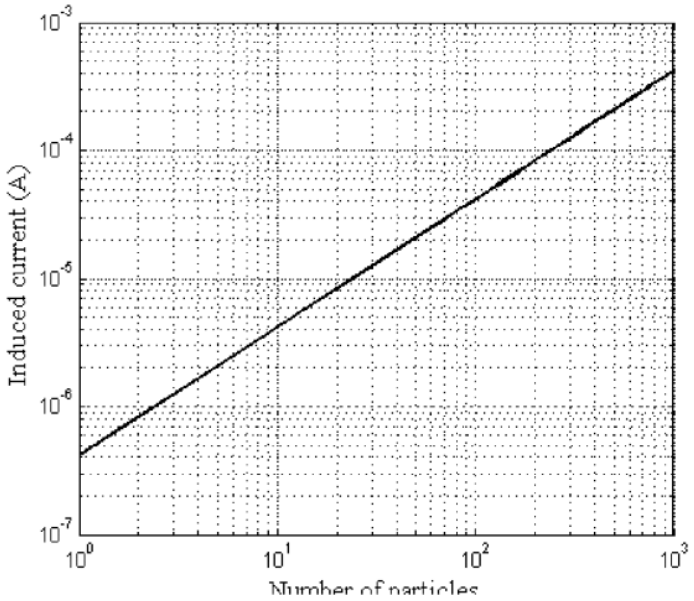

Figure 2.10: *Simulation results of the article regarding the induced current in the differential system with respect to the number of nanoparticles*

If the goal is to develop a highly sensitive sensor that can provide fast and accurate measurements, with no portability or cost constraints, then this might prove to be a perfectly viable solution to magnetic nanoparticles detection. Indeed, if this solution were to be used in a laboratory where all the necessary equipment was available to measure tiny signals and to generate an excitation signal at high frequency, this system might offer very good performance. But first, it would need to be validated in conditions similar to the one described in the article, with micrometer scale inductors.

However, if the aim is to develop a sensor that can be built with off-the-shelf components, to be used in point-of-care situations, this solution is not suitable. The challenges, be it in terms of signal generation, power consumption, or size of the inductors necessary for an accurate detection, are too big, making this solution not viable in this case. The next chapter is dedicated to the development of another, very promising solution using an LC-oscillator, which avoids most of these problems.

Chapter 3

Detection by measuring a frequency variation in a LC-oscillator

3.1 Oscillator-based sensor interfacing and frequency counting

As expressed several times so far, one of the main objectives is to develop a portable low-cost solution to nanoparticle detection, that can be built from off-the-shelf components. We thus looked at another way to interface an inductive sensor, requiring few components but that can still detect tiny changes in the self-inductance of the sensor.

Using oscillators to interface sensors is a common practice, and basic ones can be built using only a few components, thus meeting the aforementioned requirement on cost. There exists a wide variety of oscillators, which makes it possible to interface several types of sensors. Resistive or capacitive sensors are often interfaced through a relaxation oscillator [30][31][32] but Wien bridges [33] or ring oscillators [34] can also be used. Meanwhile, inductive sensors can be interfaced through LC resonance-based oscillators, such as simple LC-oscillators [35] [36] or Colpitts oscillators (CO) [37]. The choice of the architecture depends on the application and on the resolution required.

In this kind of interfacing, the oscillator is designed in such a way that its frequency of oscillation depends on the value of a component, i.e. its resistance, capacitance, or inductance, and this component value itself depends on the physical quantity one wants to measure (Temperature, humidity, etc). This enables to translate a change in this physical quantity into a measurable frequency variation. Among the existing techniques to determine the frequency of a signal, frequency counting is a commonly used method, especially since it does not require any expensive equipment [38]. A very basic microcontroller costing less than thirty euros, such as a Teensy or an Arduino, can already yield results with high precision.

We decided to explore this solution for the detection of nanoparticles, by interfacing an inductor whose inductance varies in the presence of nanoparticles, with a simple oscillator. A microcontroller Teensy then measures the frequency using a basic frequency counting technique. The objective is first to see what limit of detection is reachable when this technique is implemented in its simplest form, then to identify ways by which this limit of detection could be improved while keeping the cost low.

Firstly, a small theoretical background on oscillator theory is given, to define the

different concepts that are used throughout the chapter. The focus then shifts to a particular case of oscillator, i.e., the Colpitt oscillator (CO), to perform a more in-depth analysis of its characteristics, and characterize an actual PCB implementation of it. Finally, an analysis of the performance of the implemented oscillator with regards to nanoparticles detection and quantification is carried out.

3.2 Theoretical background on oscillators

There exist many different architectures of oscillators that can generate a wide variety of signals, each with its own working principle. Regarding our specific application, there are some constraints narrowing the choice down to only a few architectures :

- The oscillation frequency must depend on the value of an inductance.
- It must be implementable with discrete components - no microfabrication allowed.
- The oscillation frequency must be stable.

The first criterion reduces the options down to LC-based oscillators. Among the different architectures of LC-oscillator, we decided to go for a harmonic feedback oscillators, as there exist several architectures based on this configuration that can be implemented with off-the-shelf components while offering good performance regarding frequency stability.
The block diagram of this type of oscillator is presented in Figure 3.1. It has to be noted that even though an input voltage is present in the figure, an actual oscillator does not have any input signal. It has only been represented to facilitate the explanation of its principle of operation.

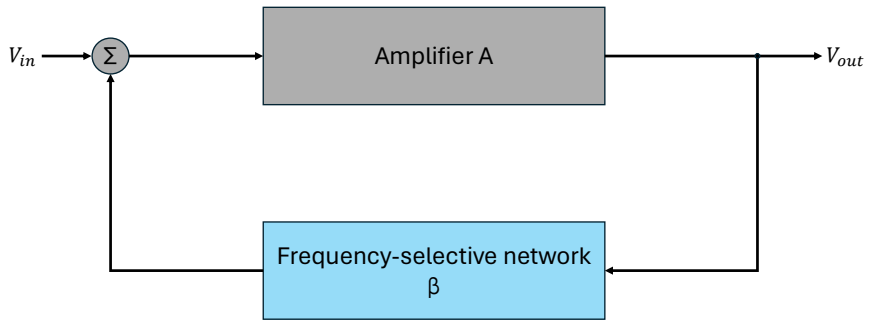

Figure 3.1: *Basic structure of a harmonic oscillator with a positive feedback loop*

This type of oscillator is composed of a frequency-selective circuit, usually a LC-tank or RC circuit, in a positive feedback loop with an amplifier. The frequency selective element fixes the oscillation frequency of the system, while the amplifier is necessary to overcome the losses in the frequency selective circuit and ensure an oscillating signal with stable amplitude.

3.2.1 Behavior analysis of a feedback oscillator

This subsection is based on Chapter 18 of *Microelectronic circuits - seventh edition*[39] and on Chapter 2 of *Frequency standards - Basics and application*[40].

The closed loop transfer function of the feedback oscillator in Figure 3.1 in closed loop is given by

$$V_{out} = \frac{A(s)V_{in}}{1 - A(s)\beta(s)} \tag{3.1}$$

where $A(s)$ is the gain of the amplifier and $\beta(s)$ the gain of the frequency-selective network. It has to be noted that the sign in the denominator of the transfer function is negative, as the feedback is positive. The loop gain of this system is then

$$L(s) = A(s)\beta(s). \tag{3.2}$$

However, by design, an oscillator does not have any input signal V_{in}. This means that to produce and sustain a finite non-zero output for a zero input signal, the gain of this system must be infinite. This condition can only be achieved if the denominator of the transfer function in closed loop is equal to 0, hence giving the condition

$$L(s) = A(s)\beta(s) = 1. \tag{3.3}$$

That is to say, at a given frequency ω_0, the phase of the loop gain must be equal to zero, and its magnitude equal to one. It should be noted that for the circuit to oscillate at one frequency ω_0, this condition should only be satisfied for one frequency. Otherwise, the output signal contains harmonics, resulting in a non-sinusoidal output signal. These requirements on the phase and the gain are also known as the Barkhausen criterion, which guarantees oscillations in a mathematical sense :

$$|\Re\{L(s)\}| = 1, \tag{3.4}$$

$$\Im\{L(s)\} = 0. \tag{3.5}$$

Frequency stability

The oscillation frequency is solely fixed by the phase characteristics of the feedback loop as the circuit can only oscillate at a frequency for which the phase of the feedback loop is zero. The stability of the oscillation frequency is thus determined by the way the phase $\Phi(\omega)$ of the loop varies around the oscillation frequency ω_0. If the derivative $\frac{d\Phi(\omega)}{d\omega}$ is large around the oscillation frequency, a large variation in the loop phase only results in a small change in ω_0. This concept is illustrated in Figure 3.2.

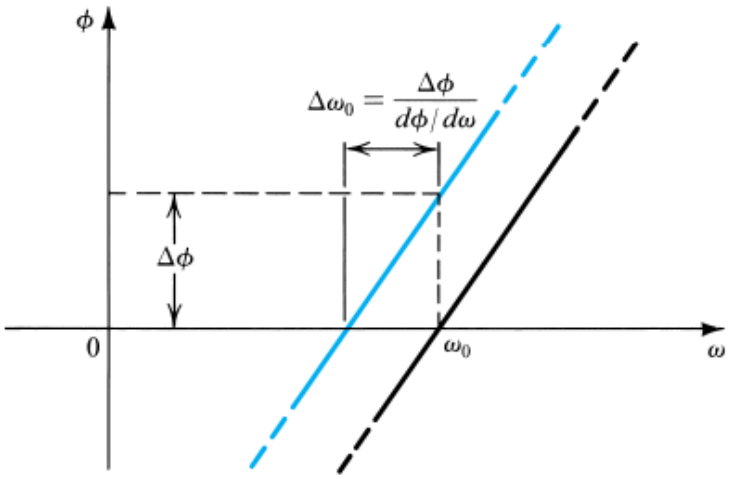

Figure 3.2: *Dependence of the oscillation frequency stability with regard to the slope of the phase response. Image from [39]*

The frequency stability of oscillators is explored in more depth later in the next section on CO.

Loop gain and amplitude control

Correctly designing the loop gain such that the circuit produces oscillations with constant amplitude is no easy task. If the loop gain is slightly lower than unity, the oscillations decay in an exponential manner until ceasing completely. Conversely, if the gain is slightly higher than unity, the circuit saturates and harmonic distortion appears.

To overcome this issue, a common practice is to design an amplifier block that has some non-linear features, by placing elements in the circuit whose characteristics depend on the amplitude of the signal applied to it. Such elements could be diodes operating in the triode region, or an amplifier with a bipolar transistor whose gain depends on the transconductance g_m of the transistor. If the input voltage becomes too large, the non-linearities of the transistor come into play to reduce the g_m, hence reducing the gain of the amplifier block and the amplitude of the oscillation.

Using such non-linear circuit in the amplifier block ensures a stable point of operation where the power P_S supplied by the amplifier exactly compensates the losses of the circuit P_D. The concept is illustrated in Figure 3.3.

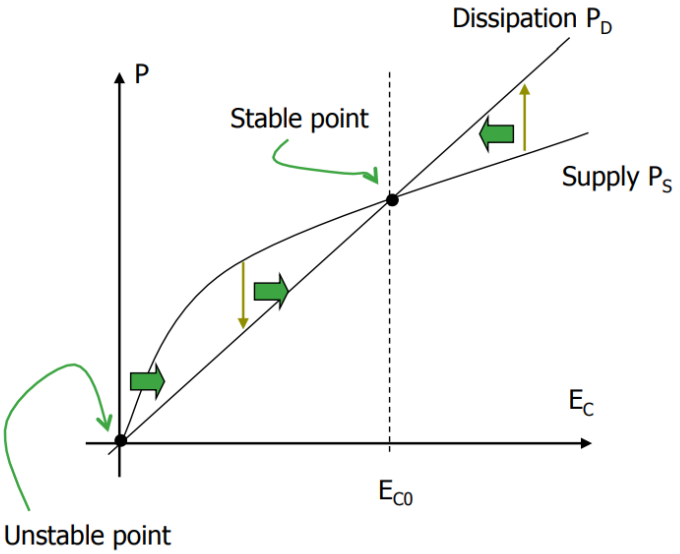

Figure 3.3: *Operating point of an oscillator with a non-linear amplitude limitation mechanism. Image from the course LELEC2532 on oscillators given by Denis Flandre at the EPL - UCLouvain [41]*

To make sure that the oscillations start when the power is turned on, the magnitude of the loop gain should be designed to be slightly greater than unity. At startup, the noise present in the circuit provides the necessary perturbation so that the circuit is not stuck at zero. The loop gain then ensures that the amplitude of the oscillation grows until the amplitude-limiting mechanism starts to play its role maintaining the amplitude constant.

Small signal analysis in open loop

In order to analyze such an oscillator, an open-loop analysis needs to be done. This enables to find the expression of the loop gain of the circuit, and thus the oscillation frequency. To perform this analysis, one must first carefully open the feedback loop. If the amplifier is built around an operational amplifier, or a transistor, a good place to open the loop is at the input of the AOP, or at the gate/base of the transistor. By calculating the small signal open-loop transfer function of the circuit, one can find the oscillation frequency by equating the imaginary part of the transfer function to zero, as well as the condition for the gain at the oscillation frequency.

3.2.2 A common architecture with its small signal analysis

Among the different architectures that exist for this type of oscillator, the one that is considered in this work is presented in Figure 3.4. It is composed of an amplification stage with a bipolar junction transistor (BJT) in a common emitter configuration, and a resonator containing three impedances Z_1, Z_2, and Z_3. The amplification stage could also be implemented with an operational amplifier, but the advantage of the BJT is that its gain-bandwidth product is much higher than a general purpose amplifier. This ensures that it does not limit the frequency of operation of the system.

The three impedances Z_1, Z_2, and Z_3 can be capacitive, inductive, or both. Depending on their type, they lead to slightly different configurations, each known under a different name and with slightly different expressions for the oscillation frequency and for the gain.

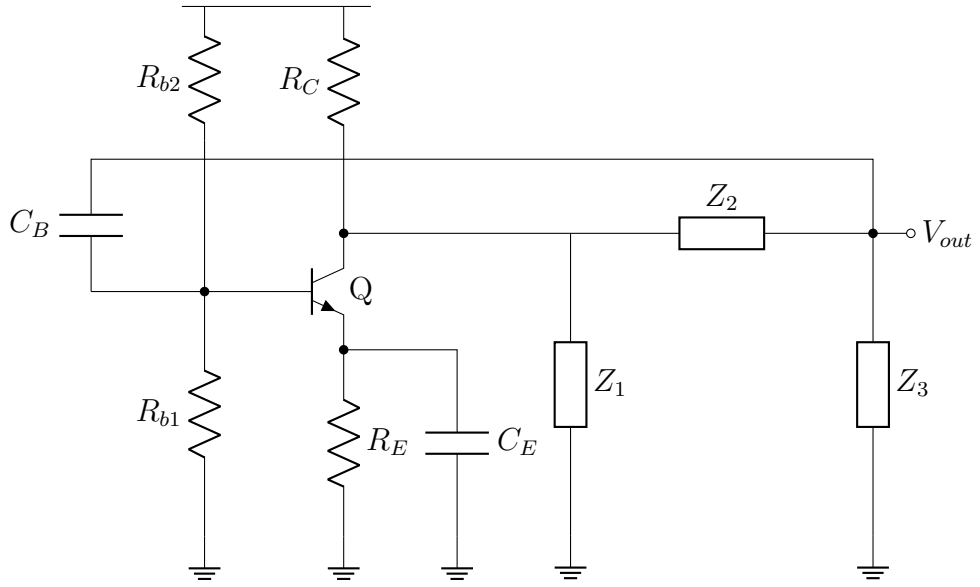

Figure 3.4: *General architecture*

For example, if Z_1 and Z_3 are capacitors and Z_2 is an inductor, it forms a CO. Conversely, if Z_1 and Z_3 are inductors, and Z_2 is a capacitor, it is known as a Hartley oscillator.

Transfer function - general case

As the circuit presented in Figure 3.4 can be derived in several configurations, it is more convenient to perform a general analysis without specifying further the nature of the impedances Z_1, Z_2 and Z_3. Their values can then be specified depending on the chosen oscillator type.

As explained previously, to analyze such a circuit, one first needs to open the loop and calculate the corresponding small signal transfer function of the resulting circuit. A sensible place to open the loop for this configuration is at the base of the transistor, as its input impedance is very high. The resulting circuit is presented in Figure 3.5, where the BJT has been replaced by its pi-model. A few simplifications are made in order to obtain this model:

- The capacitors C_E and C_B are coupling capacitors, and are thus very large. They behave as short circuits in the small signal configuration and can then be replaced by a simple wire.
- The sole purpose of R_{b1} and R_{b2} is to set the DC operating point of the transistor, they can also be neglected in the small signal analysis (see appendix A for a more detailed study of their influence).
- The transistor is considered ideal, its base current is then equal to zero, and its parasitic capacitances are neglected as they only play a role at much higher frequencies than the oscillation frequency.

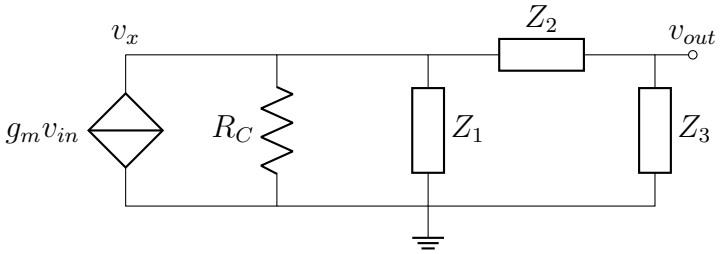

Figure 3.5: *Small signal circuit for the oscillator in open loop. C_E and C_B have been replaced by short circuits.*

Using Kirchhoff's current law, two equations can be derived at the node v_x and the node v_{out} :

$$\frac{v_{out} - v_x}{Z_2} = \frac{v_x}{Z_1} + \frac{v_x}{R_C} + g_m v_{in}, \tag{3.6}$$

$$-\frac{v_{out}}{Z_3} = \frac{v_{out} - v_x}{Z_2}. \tag{3.7}$$

By rearranging the two equations to isolate $\frac{v_{out}}{v_{in}}$, the following transfer function is obtained:

$$\frac{v_{out}}{v_{in}} = -\frac{g_m Z_1 Z_3 R_C}{Z_1(Z_2 + Z_3) + R_C(Z_1 + Z_2 + Z_3)}. \tag{3.8}$$

If the impedances Z_1, Z_2, and Z_3 are purely imaginary, i.e., capacitive $Z = \frac{1}{j\omega C}$, inductive $Z = j\omega L$, or both, the oscillation conditions can be written. To find the oscillation frequency, the following equation must be solved for ω

$$Z_1 + Z_2 + Z_3 = 0, \tag{3.9}$$

and to ensure sustained oscillation, the following condition has to be met at the oscillation frequency:

$$g_m R_C = 1 + \frac{Z_2}{Z_3}. \tag{3.10}$$

3.3 The Colpitts oscillator

The CO is a particular case of the architecture presented in the previous section. It was invented about a hundred years ago by E. H. Colpitt, and is known for remarkable performance regarding phase noise and frequency stability [42]. Since its invention, many variations have been proposed [43], to improve its performances even more by using new technologies, for the amplification stage, for example.

As a first approach, we decided to implement a CO in its original form, which is the topology presented in Figure 3.4, with Z_1 and Z_3 that are capacitors, and Z_2 that is an inductor. There are two main reasons for this choice. The first one is that, contrary to the Hartley oscillator, where both Z_1 and Z_3 are inductors, the CO features only one inductor, which makes it ideal to interface an inductive nanoparticle sensor. The second is because the original CO can be implemented with a BJT, whereas many of its variants are using the CMOS technology, hence requiring microfabrication.

The objective with this first implementation is to characterize the performance of a simple oscillator in the context of nanoparticles detection by frequency counting. This enables us to get an order of magnitude for the limit of detection reachable with this kind of system, when it is implemented with discrete components. Once this characterization is carried out, it is possible to identify the bottlenecks of this technique and identify the possible improvements.

3.3.1 Theoretical analysis of the Colpitts oscillator

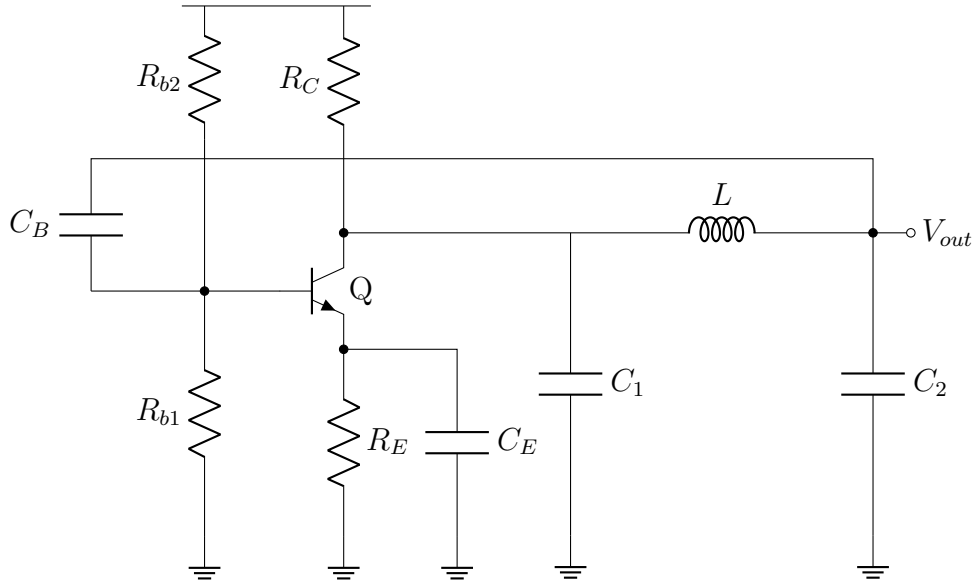

Figure 3.6: *Colpitt oscillator*

The complete circuit of the CO is presented in Figure 3.6. Based on (3.8), its transfer function can be computed by replacing the impedance Z by their corresponding value. In a CO, Z_1 and Z_3 are capacitors, and Z_2 is an inductor, yielding:

- $Z_1 = \frac{1}{j\omega C_1}$,
- $Z_2 = j\omega L$,
- $Z_3 = \frac{1}{j\omega C_2}$.

Replacing these values in the general transfer function, it becomes:

$$\frac{v_{out}}{v_{in}} = \frac{g_m R_C}{1 - \omega^2 L C_2 + j\omega R_C(C_1 + C_2 - \omega^2 L C_1 C_2)}. \tag{3.11}$$

In order to have an oscillation, the two conditions given by the Barkhausen criterion must be met. The oscillation frequency corresponds to the frequency for which the imaginary part of the transfer function (3.3.1) is equal to zero:

$$\Im\left\{\frac{v_{out}}{v_{in}}\right\} = R_C(C_1 + C_2 - \omega L C_1 C_2 = 0, \tag{3.12}$$

which gives the following expression for the oscillation frequency ω_0:

$$\omega_0 = \sqrt{\frac{C_1 + C_2}{L C_1 C_2}}. \tag{3.13}$$

The second criterion states that the magnitude of the transfer function at ω_0 must be equal to one, giving the following condition:

$$\Re\left\{\frac{v_{out}}{v_{in}}\right\} = \frac{g_m R_C}{1-\omega_0^2 L C_2} = 1. \tag{3.14}$$

Replacing ω_0 by its expression (3.3.1) in (3.3.1), it gives

$$g_m R_C = \frac{C_2}{C_1}, \tag{3.15}$$

where one can recognize the expression of the gain of a bipolar amplifier in a common emitter configuration $g_m R_C$. In practice, the amplifier is designed to have a gain slightly superior to the ratio of the two capacitors, to ensure that it can compensate all the losses in the circuit and that the oscillations start. As the gain of the amplifier depends on the transconductance, it stabilizes around unity at the oscillation frequency.

For a bipolar transistor, the transconductance can be calculated with

$$g_m := \frac{I_C}{V_T} \tag{3.16}$$

with I_C the bias current through the collector and $V_T = \frac{kT}{q} = 26$ mV at 25°C. As the transistor needs to be in the active regime for the oscillator to work, $V_{BE} \approx 0.7$ V, and V_B being fixed by the resistors R_{b1} and R_{b2}, the I_C current can easily be found, giving

$$g_m = \left(\frac{V_{dd} R_{b2}}{R_{b1}+R_{b2}} - 0.7\right) \times \frac{1}{R_E V_T} \tag{3.17}$$

The base current has been neglected in this expression as the transistor is considered ideal. The open-loop transfer function of the CO is shown in Figure 3.7. The oscillation frequency is at the peak around 320 kHz.

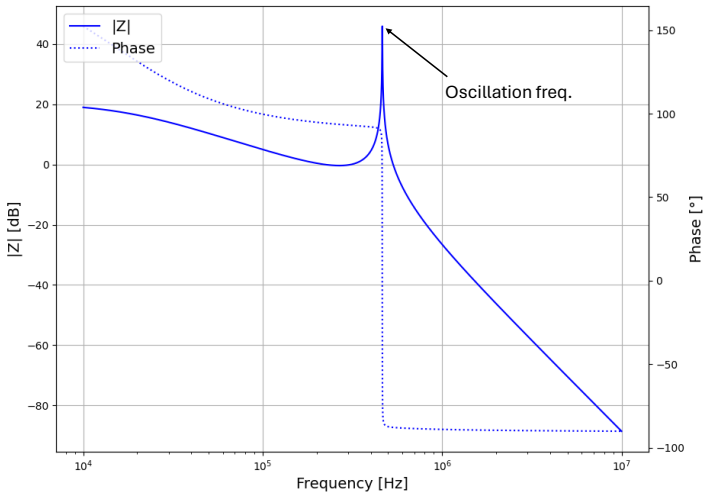

Figure 3.7: *Open loop transfer function of the CO. $L = 5$ μH - $C_1 = C_2 = 100$ nF.*

3.3.2 Q-factor

An important figure of merit in an oscillator is its quality factor Q, which gives an indication of the stability of the oscillation frequency. The higher the Q, the more stable the

frequency of oscillation is. The Q factor of an oscillator or a resonator is a dimensionless parameter that describes how underdamped the system is. In the context of resonators or oscillators, two definitions are commonly used for Q, giving similar though not perfectly equal results [44].

The first definition is relative to the ratio between the energy stored in the resonator and the energy lost per cycle.

$$Q \coloneqq 2\pi \times \frac{\text{energy stored}}{\text{energy dissipated per cycle}} = 2\pi f_0 \times \frac{\text{energy stored}}{\text{power loss}}, \tag{3.18}$$

where f_0 is the resonant frequency.

The second definition is related to what is called the resonance width, i.e., the bandwidth over which the power of oscillation is greater than half of the power of the resonant frequency. The definition of Q using this concept is then

$$Q \coloneqq \frac{f_0}{\Delta f} = \frac{\omega_0}{\Delta \omega} \tag{3.19}$$

Where Δf is the resonance width. Figure 3.8 illustrates this frequency definition, as well as the concept of resonance width.

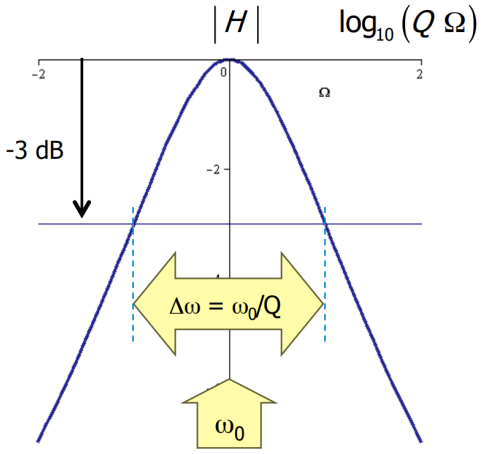

Figure 3.8: *Illustration of the frequency definition of the Q factor and the concept of resonance width. $|H|$ is the open loop transfer function of the oscillator. Image from [41].*

Intuitively, the first definition expresses the frequency stability by looking at the gain of the transfer function, and how high is the peak at the resonance. The higher the losses in the circuit, the smaller the gain is at the oscillation frequency, and the smoother the peak is. As a result, there is a wider range of frequencies with a similar level of amplification around the oscillation frequency, as can be seen in Figure 3.9a. The resulting output signal of the oscillator would contain other frequencies, making it less stable.

The second definition would be more related to the phase change at the oscillation frequency. The narrower the resonance width, the sharper the phase change is. As illustrated in Section 3.2.1, a sharp phase variation means that a change in the phase of the loop only causes a small change in the oscillation frequency. Figure 3.9b shows the phase response of the open-loop transfer function for different values of Q, where it can be observed that the higher the Q is, the sharper the phase variation is.

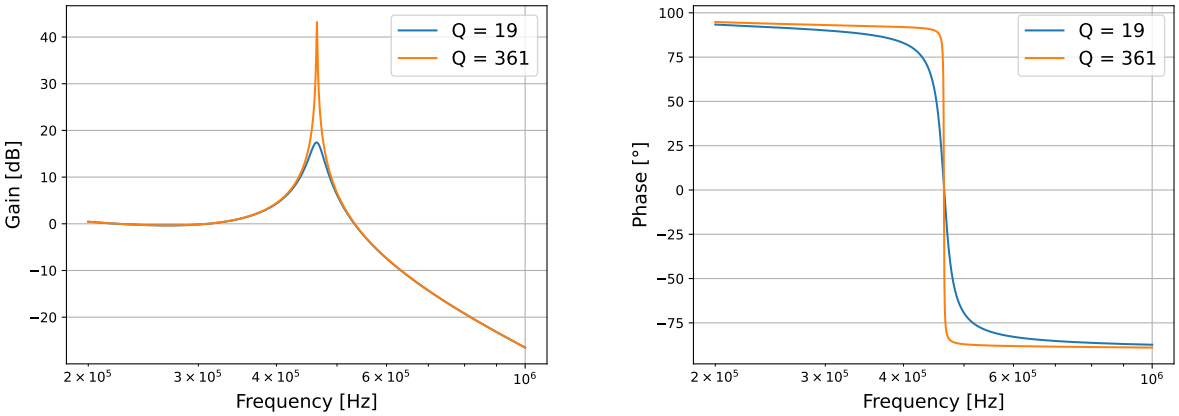

(a) *Amplitude of the open loop transfer function* **(b)** *Phase of the open loop transfer function*

Figure 3.9: *Open loop transfer function of the Colpitt*

3.3.3 Impact of the series resistance of the inductor on Q

In an LC-oscillator the Q factor of the resonator is not the same as the Q factor of the entire oscillator. For example, an oscillator can have a very high Q resonator, but the non-linear circuit around it could introduce a lot of distortion and power losses if poorly designed. This would result in a low-Q oscillator, despite having a high-Q resonator [44]. However, we assume that, as the CO has remarkable frequency stability, the circuit was designed in such a way that the amplifier block does not introduce too much distortion or power losses. The overall Q of the oscillator then mostly depends on the Q of the resonator.

As the energy definition (3.3.2) of Q states, in order to have a good quality factor, one needs to minimize as much as possible the energy dissipated in the circuit while maximizing the energy stored. The main dissipative element in the resonator, which then has to be minimized, is the series resistance of the inductor. More specifically, it is the ratio $\frac{L}{R_L}$ that is important, i.e., the inductance needs to be large with respect to its series resistance. The larger the inductance, the more energy it can store. The smaller its series resistance is, the less energy it dissipates.

The impact of R_L can be taken into account in the overall transfer function by setting the impedance value Z_2 from the general circuit 3.4 to

$$Z_2 = R_L + j\omega L. \tag{3.20}$$

The impedances Z_1 and Z_3 keep the same value as before. The new transfer function taking into account R_L can be computed, leading to the following conditions for the Barkhausen criterion, with the additional terms due to R_L in blue:

For the imaginary part

$$\Im\left\{\frac{v_{out}}{v_{in}}\right\} = \omega\Big[R_C(C_1 + C_2 - \omega^2 LC_1C_2) + \color{blue}{R_LC_2}\Big] = 0. \tag{3.21}$$

For the real part

$$\left|\Re\left\{\frac{v_{out}}{v_{in}}\right\}\right| = \left|\frac{g_m R_b R_C}{1 - \omega_0^2(LC_2 + \color{blue}{R_C R_L C_1 C_2})}\right| = 1. \tag{3.22}$$

Again, the oscillation frequency taking into account R_L can be determined with the first condition, giving

$$\omega_0 = \sqrt{\frac{C_1 + C_2}{LC_1C_2} + \frac{R_LC_2}{R_CLC_1C_2}}. \tag{3.23}$$

However, since the additional term due to R_L is several orders of magnitude smaller than the other term, it can be neglected. The value of the theoretical oscillation frequency is thus barely impacted by the series resistance of the inductor.

The impact of R_L on the real part of the transfer function is much more significant, as it introduces a non-negligible term in the expression of the gain at ω_0. This additional term being in the denominator of the transfer function, it causes the gain to drop significantly as R_L increases.

The impact of R_L on Q and the loop gain is simulated for a CO with an inductor of 10 µH by performing a sweep on the value of R_L and extracting the corresponding Q factor. The results of this simulation are shown in Figure 3.10. The Q factor was calculated using its bandwidth definition. As shown in the figure, both the gain and the Q vary in a very similar manner with regard to the series resistance of the inductor. It demonstrates the importance of trying to minimize R_L as much as possible relative to the inductance L, or equivalently, maximize the ratio $\frac{L}{R}$.

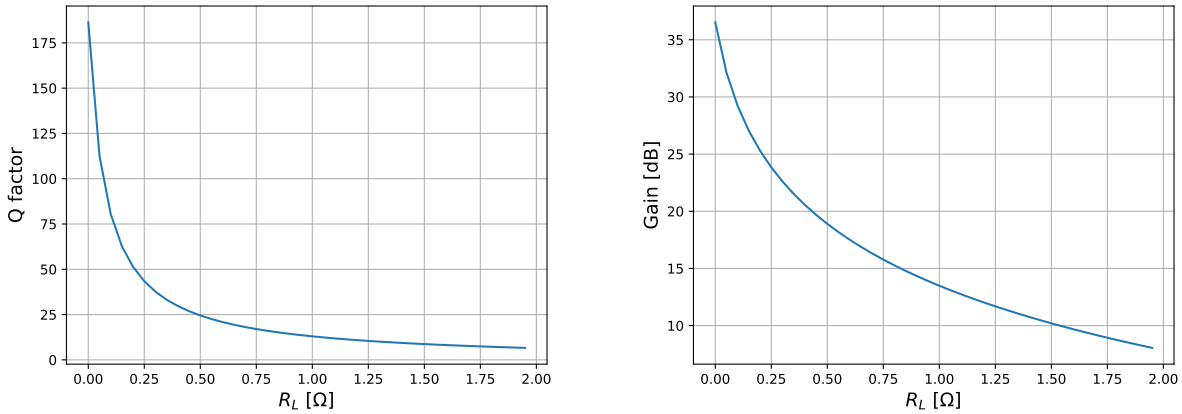

(a) *Q vs* R_L **(b)** *Gain vs* R_L

Figure 3.10: ***LTSpice simulation : Impact of*** R_L ***on the Q-factor (a) and on the gain (b)*** *for a CO with* $L = 10\ \mu H$, $C_1 = C_2 = 100nF$ *and* R_L *ranging from 0 to 2* Ω

Looking at the energy definition given by Eq. (3.3.2) of the Q factor, this makes perfect sense. By increasing R_L, the energy dissipation in the circuit also increases, reducing its quality factor. To demonstrate this, one can write the Q factor of the resonator,in the CO, which is a simple LC-tank. In such a system, the energy is alternatively stored as magnetic energy and electrical energy in the inductor and the capacitor, respectively. Therefore, to obtain the total energy stored in the LC tank, one can write the expression of the energy E_L that can be stored in the inductor

$$E_L = \frac{LI_{ind}^2}{2}, \tag{3.24}$$

with I_{ind} the current passing through the inductor. When I_{ind} is at its maximum, it means that all the energy of the system is currently stored in the inductor. On the other hand, the

energy dissipated by R_L can be written as

$$E_R = \frac{R_L I_{ind}^2}{2}. \tag{3.25}$$

The factor $\frac{1}{2}$ comes from the fact that the RMS value of the current is considered:

$$I_{RMS} = \frac{I_{ind}}{\sqrt{2}}. \tag{3.26}$$

Using (3.3.2), the following expression can be derived:

$$Q = \omega \times \frac{E_L}{E_R} = \omega \frac{L}{R_L} \tag{3.27}$$

As expressed by this equation, to maximize the Q-factor of the resonator, the ratio L over R_L has to be maximised.

3.3.4 Phase noise

Phase noise is an important metric in the characterization of an oscillator, as it describes the spectral purity of its oscillations [45]. It is the frequency counterpart of the jitter[46] and is often expressed in dBc/Hz, i.e., the noise power relative to the carrier at a given offset from the carrier and over a given bandwidth (usually 1 Hz). It can be calculated using the following expression:

$$\mathcal{L}(\Delta\omega) = 10 \log_{10} \left(\frac{S_v(\omega_0 + \Delta\omega)}{P_0} \right), \tag{3.28}$$

where $\mathcal{L}(\Delta\omega)$ is the phase noise at an offset $\Delta\omega$ from the carrier in dBc/Hz, and $S_v(\omega_0 + \Delta\omega)$ is the power of the noise at the given offset, normalized by the power of the carrier P_0. Many phase noise models have been developed over the years to predict the phase noise of a circuit [45], some as early as 1966 with the Leeson model [47], which has paved the way for many studies on the subject.

The objective of this section is not to develop an accurate model of the phase noise of the CO, but instead giving an intuition on the effect of phase noise, and suggesting ways to improve it. The model proposed by D. Ham and al. in their article *"Phase noise in oscillators"* [48] gives this intuition, and the remainder of this subsection is based on the discussion they propose. Unless specified otherwise, all the figures of this subsection come from this article.

A generic model for a self-sustained LC-oscillator is presented in Figure 3.11. This circuit is used as the base case to discuss the concept of phase diffusion.

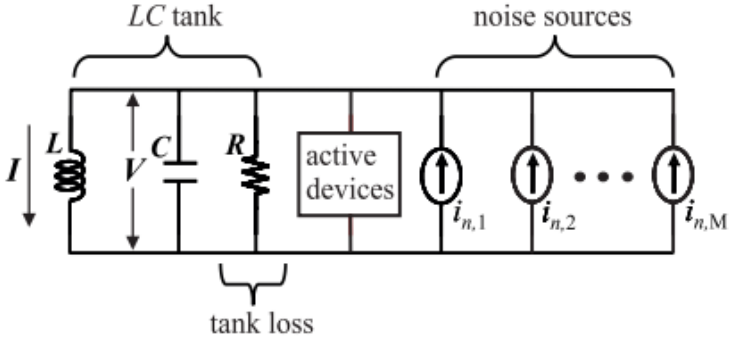

Figure 3.11: *Generic model for a self-sustained LC-oscillator*

In this circuit, the LC tank acts as the frequency selective network while the active devices ensure a sustained oscillation by compensating for the losses in the tank. The resonator losses due to R and the active devices generate noise that is represented through the current sources.

The dynamics of the LC oscillator can be represented on a graph showing the relationship between the voltage V across the capacitor, and the current I going through the inductor. Plotting this relation over time forms a trajectory in the V-I space, illustrated in Figure 3.12. In steady-state, this trajectory forms a closed curve due to the periodicity, and is called a limit cycle. Regardless of the starting point, the system always evolves towards this limit cycle after a transient state. Due to this dynamic, the amplitude of oscillation of a self-sustained oscillator is very stable as it is always drawn to the limit cycle.

However, there is no such mechanism controlling the fluctuations in the direction along the limit cycle to force the phase to its original value. As a result, in the presence of noise, the state point slowly deviates from its original phase by moving randomly along the limit cycle. The phase undergoes what is known as a "diffusion" process.

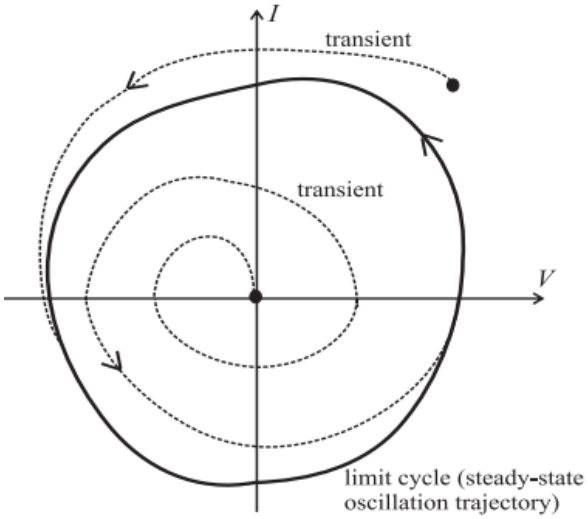

Figure 3.12: *Limit cycle in the V-I state space*

The fundamental component of the voltage produced across the LC tank can be modelled as

$$V(t) = V_0 \cos[\omega_0 t + \phi(t)], \tag{3.29}$$

where ω_0 is the oscillation frequency, V_0 the amplitude of oscillation, and the term $\phi(t)$ accounts for the phase fluctuations, assuming a diffusion process as explained earlier. If this phase diffusion is due to white noise, its variance can be calculated with

$$\langle \phi^2(t) \rangle = 2Dt \tag{3.30}$$

where D is the phase diffusion constant, indicating how fast the diffusion occurs. The greater it is, the faster the phase diffuses, and the higher the phase noise is. It is actually the sole factor determining the oscillator phase noise. The power spectral density of the signal produced by the oscillator is then given by the Lorentzian

$$S_V(\omega) = V_0^2 \frac{D}{(\Delta\omega)^2 + D^2}. \tag{3.31}$$

The larger the D, the more widely the energy is distributed around the carrier frequency for a fixed oscillator energy. Figure 3.13 shows the power spectral density of the output signal of the oscillator with different values of D.

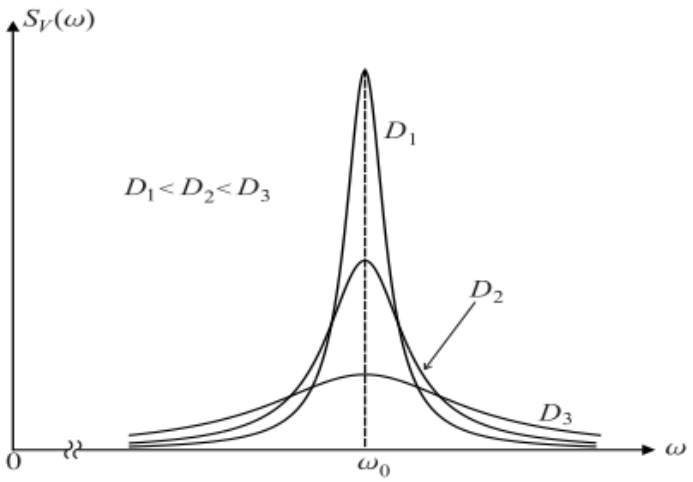

Figure 3.13: *Power spectral densities of the oscillator output signal for different diffusion constants for the same oscillation energy*

The definition of this diffusion constant D is then crucial to getting an accurate model of the phase noise, especially since this system is not linear time invariant (LTI). This has to somehow be taken into account in the definition of D. The article proposes such a definition, and it is actually one of the major improvements with regards to the model proposed by Leeson [47], as the Leeson model does not accurately model linear time variant systems (LTV)[45].

However, for the sake of simplicity, the time-varying effects are ignored, as it still enables to see which parameters affect the phase noise performance while keeping the math simple. Under this hypothesis, D can be expressed as

$$D = \frac{Q}{Q_{eff}} \cdot \frac{k_B T}{2P_s} \cdot \frac{\omega_0^2}{Q^2}, \tag{3.32}$$

where Q is the quality factor of the resonator such as defined in the previous section, and P_s is the power dissipation in the resistive part of the resonator. Q_{eff} can be seen as a measure of the noise present in the circuit, taking into account both the thermal and the shot noise. It is defined by the authors of the article as

$$Q_{eff} \equiv (R_1||R_2||...||R_M)C\omega_0, \tag{3.33}$$

where R_1, R_2, ..., R_M are the corresponding equivalent resistances modeling the noise contribution of each noise source (that is not necessarily thermal). From (3.3.4), it is evident that an efficient way to minimize the phase noise of a LC-oscillator, is to minimize the losses in the circuit and to design an LC tank with a quality factor as high as possible.

Figure 3.14 shows the typical phase noise of an oscillator as a function of the offset from the carrier. There is a first region where the phase noise varies with a slope of -30 dB per decade. This corresponds to the region where flicker noise dominates. It then passes in the $1/f^2$ region, where the slope is -20dB per decade, which corresponds to the region where phase noise is mostly caused by thermal noise.

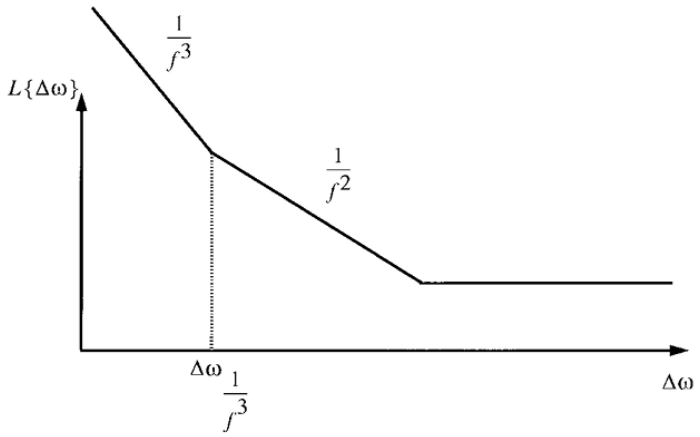

Figure 3.14: *Typical phase noise of an oscillator as a function of the offset from the carrier. Image from [49]*

3.4 Simulation and characterization of the Colpitt oscillator

To get a first idea of the limit of detection (LoD) reachable with a basic implementation of such system, and to study the impact of the parameters of the inductor on this LoD, a basic CO was implemented on Printed Circuit Board (PCB). Several identical PCB are printed, and regarding the components used for these circuits, the inductor is the only one that is different from one circuit to another. A detailed description of these inductors is given in section 3.4.2.

3.4.1 Sizing of the circuit

The names of the components refer to the circuit 3.6 presented at the start of Section 3.3.1. The resonator block refers to the frequency-selective block of a feedback oscillator while the amplifier block refers to its amplifier block.

Resonator block

By choosing $C_1 = C_2 = C_{res}$, one can simplify even more the expression for the oscillation frequency of the CO, leading to

$$\omega_0 = \sqrt{\frac{2}{LC_{res}}} \tag{3.34}$$

Given that the inductors used have inductance values ranging from 2.5 µH to 27.5 µH, the value of C_{res} is set to 100 nF to keep a frequency of oscillation below 500 kHz. Working at higher frequency would require components with higher transition frequency, especially in the conditioning chain picking up the signal from the oscillator for post-processing. These components are usually more expensive and consume more power.

Amplifier block

The capacitors C_E and C_B are coupling capacitors, and their role is to block the DC component of the signal while still transmitting the AC component. They need to be large

enough, so that their impedance at the oscillation frequency is small enough to be considered as a short circuit. The lowest frequency of oscillation we obtain with the value of components in the resonator is around 120 kHz, setting $C_E = C_B = 1\mu F$ is then a reasonable choice.

As a reminder, the Barkhausen criterion states that the following condition on the gain must be met at the oscillation frequency:

$$g_m R_C = \frac{C_2}{C_1} \tag{3.35}$$

Taking $R_C = 2.2k$ gives a gain higher than unity, ensuring that the amplifier is able to provide enough gain to overcome all the losses in the circuit.

To work as an amplifier, the transistor needs to be in the active regime, meaning that the following conditions must then be respected:

$$V_{BE} \approx 0.7V < V_{CE}, \tag{3.36}$$

$$V_{CB} > 0V. \tag{3.37}$$

Setting the base voltage $V_B = \frac{V_{dd}}{3}$ ensures that both conditions are met, and we chose $R_{b1} =$ 100 kΩ and $R_{b2} = 51$ kΩ to fix this voltage. Finally, R_E was set to 1 kΩ.

Table 3.1 summarizes the values of the components used in the circuit. The same values are used throughout all the circuits, with he only varying parameter being the inductor.

Component name	**Value**
R_{b1}	100 kΩ
R_{b2}	51 kΩ
R_C	2.2 kΩ
R_E	1 kΩ
C_E & C_B	1 µF
Transistor Q	NPN - BC107B
C_1 & C_2	100 nF

Table 3.1: ***Value of the components*** *that are identical throughout all the circuits*

3.4.2 Characterization of the inductors

Supports for the coils

The supports on which the inductor coils are wound are shown in Figure 3.15. These are 3D-printed with the Clear V4 resin from FormLab.

Figure 3.15: *Support for the inductor coil that are used*

The shape of the core is elliptical to ease the introduction of the paper sample on which the nanoparticles are deposited, while minimizing the void at the center of the coil. This enables us to maximize the influence of the nanoparticles on the value of the inductance, since the latter depends on the magnetic permeability of the core.

To wind the copper wire on the support, a small setup with a motor was used, and the purpose of the element framed on the front view of 3.15 is to fix the support on the motor shaft. To clamp the coil support on the edge of the PCB, the element framed on the left view of Figure 3.15 was also added. This ensures that the coil is correctly fixed on the PCB and that the measurement will not be disturbed by unwanted movements of the support.

LCR measurements

The impedance of the inductor is first measured using the LCR 4284A II from Agilent. The measurement frequency of this device ranges from 20 Hz to 1 MHz, which enables us to get an accurate measurement of the series resistance of the coils. The usual model of an inductor is shown in Figure 3.16. The resistor R_L models the series resistance of the wire used to fabricate the inductor while the capacitor C_p models the stray capacitance between the wire turns.

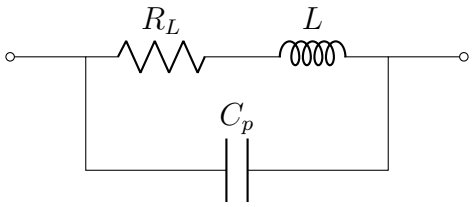

Figure 3.16: *Model of an inductor with the parasitic series resistance R_L and the parasitic capacitor C_p*

The total impedance Z of this model is

$$Z = \frac{R_L + j\omega L}{1 + j\omega R_L C_p - \omega^2 L C_P}. \tag{3.38}$$

At low frequencies, i.e., smaller than the self-resonant frequency of the inductor, the capacitor does not have any impact and can be neglected. When the series resistance is higher than the module of the impedance of the inductance, the total impedance behaves in a resistive manner. When the frequency increases, the impedance of the inductor progressively increases until it is equal to the value of R_L. At that point, the inductive behavior takes over the resistive behavior, causing the phase to shift from zero to ninety degrees. The impedance then reaches a maximum value at $\omega = \frac{1}{\sqrt{LC_p}}$, which is the self-resonance peak. At that point, the behavior becomes capacitive and the total impedance decreases with frequency, as the capacitor acts like an AC-short circuit. Figure 3.17 shows the typical evolution of the module and the phase of the impedance of an inductor over a wide frequency range.

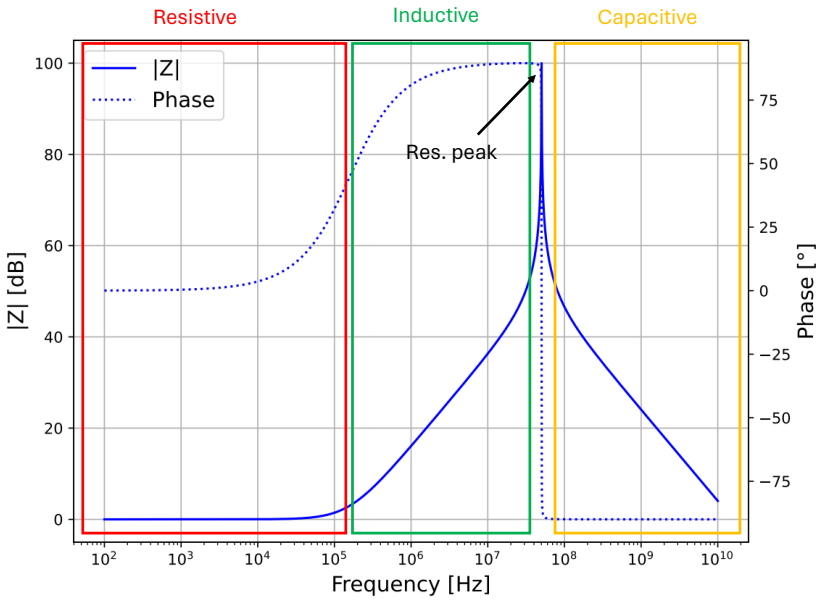

Figure 3.17: ***Typical |Z| - θ curve of an inductor.*** *Calculated for $L = 10\ \mu H$, $R_L = 1\ \Omega$ and $C_p = 10\ pF$. The different regions are framed in different colors, and the self-resonance peak is pointed by the arrow.*

When Z shifts from a resistive behavior to an inductive behavior, there is a point where

$$R_L = j\omega L, \tag{3.39}$$

and where the phase is equal to 45°. Knowing this, it is possible to extract the value of R_L by extracting the value of Z at that point. If C_p is neglected, we can write the following for the modulus of Z, to extract the value of R_L

$$|Z_{45}| = \sqrt{R_L^2 + (\omega L)^2} \tag{3.40}$$

$$= \sqrt{2} R_L. \tag{3.41}$$

The values of the series resistance of the inductors used in this work are listed in Table 3.2. These values are extracted from the LCR curve obtained for each of them, as explained in this section.

Impedance analyzer measurements

The inductance of the coils is measured using the impedance analyzer E4991B from Keysight Technologies. This device is complementary to the LCR regarding the frequency range over which it operates. The LCR is able to perform measurement at frequencies as low as 20 Hz, which is ideal to get an accurate measurement of the series resistance of the coils. However, it cannot cover frequencies higher than 1 MHz, which limits its ability to accurately measure small inductance values. On the other hand, the Impedance Analyzer E4991B can cover a frequency range from 1 MHz to 3 GHz. This makes it ideal to measure the inductance and the parasitic capacitance of a coil, but it is less effective in determining the series resistance.

The inductance value can be extracted based on the frequency response of the impedance. When the behavior of the inductor is inductive, its impedance varies linearly with frequency and is equal to

$$|Z| = R_L + j\omega L \tag{3.42}$$

L can then be extracted by picking a point (f_L, Z_L) in the inductive region, giving

$$L = \frac{|Z_L| - R_L}{2\pi f_L} \tag{3.43}$$

The inductance value of the coils used in this work are listed in Table 3.2. Each measure was taken five times to get an idea of the variability of the measurement.

Inductors used in this work

Three different pairs of inductors, L_{11}/L_{12}, L_{21}/L_{22} and L_{31}/L_{32} are used in this work. Each pair is designed to have the same inductance, but the wire used has a different section, therefore changing the ratio $\frac{L}{R}$. Even though the wires are wound around an elliptical center and not a circular one, the value of the inductance that is obtained with the supports used in this work can be roughly estimated with the formula for a solenoid

$$L = \mu \frac{AN^2}{l} \tag{3.44}$$

with μ the magnetic permeability of the material of the core, A the cross-section area, l the length of the solenoid, and N the number of turns. This estimation is not very accurate, especially when N is high, but it gives an order of magnitude on the value of L.

!The aim is to have inductance values around $L_{11}/L_{12} = 2.5\mu H$, $L_{21}/L_{22} = 10\mu H$, and $L_{31}/L_{32} = 20\mu H$. Using (3.4.2) and the dimensions of the supports, this gives $N_{11}/N_{12} = 31$, $N_{21}N_{22} = 63$ and $N_{13}/N_{23} = 90$. The objectives with these six inductors are multiple:

- Validate the relationship between the frequency and the inductance value found in the theoretical analysis of the CO.
- Determine whether the inductance value has an influence on the system limit of detection.
- Determine the impact of the L/R ratio on the frequency stability and on the limit of detection.

Inductor	**Value [µH]**	σ of L [nH]	**Wire section [mm^2]**	R_L [Ω]	N
L_{11}	3.2669	0.0906	0.049	0.3245	30
L_{12}	3.1384	0.1338	0.159	0.106	30
L_{21}	13.658	0.2728	0.049	0.6594	63
L_{22}	14.658	0.2748	0.159	0.224	63
L_{31}	27.553	0.6552	0.049	0.9325	90
L_{32}	29.992	0.0073	0.159	0.4199	90

Table 3.2: ***Parameters of the inductors*** *that are used to characterize the first design. The inductance value is measured using the VNA, and the series resistance using the LCR. It can be noted that the standard deviation σ is smaller than 1 nH, meaning that there is little variability between the measurements.*

The error between the theoretical value of L given by the formula (3.4.2) is relatively high, but the order of magnitude is the same, and it does not impact our objective. Also, the VNA seems to produce measurements with very little variability, as the standard deviation σ over five measures is less than one nH.

3.4.3 Analysis of the frequency content of the oscillator signals

The instrument for the phase noise analysis was unavailable at the moment of measurement, but it is still possible to analyze the frequency content of the signals from the oscillators by using a one-sided power spectral density (PSD). This enables, among other things, to determine the purity of the signal and detect the presence of harmonics. The purer the frequency content of the signal is, the more stable it is.

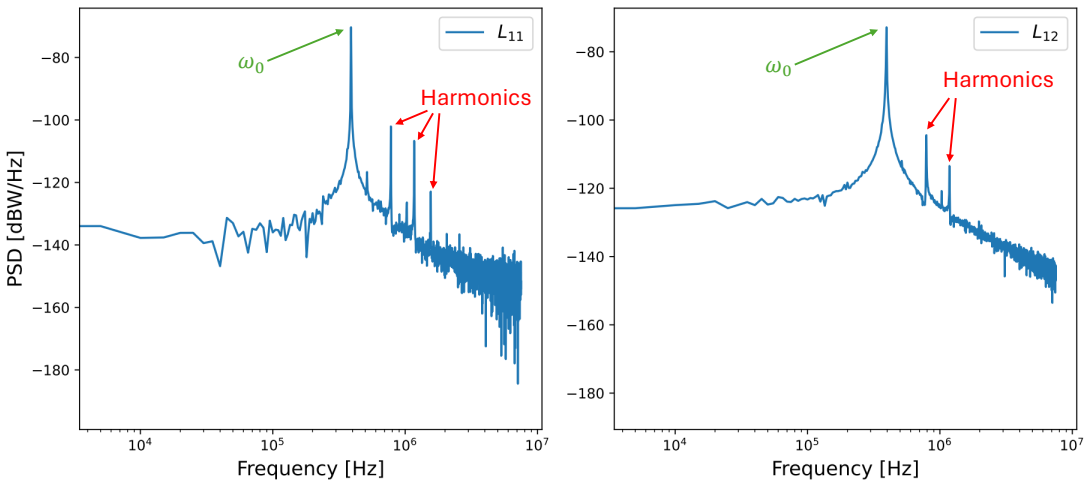

Figure 3.18: *PSD of the signal from L_{11} (left) and L_{12} (right). The harmonics are pointed by the red arrows, and the oscillation frequency ω_0 is pointed by the green ones*

Figure 3.18 illustrates the PSD of the L_{11} and L_{12} oscillators. It can be observed that the spectrum of L_{12} is purer than the spectrum of L_{11}, probably due to the lower series resistance of the inductor. It contains less harmonics and their amplitude relative to the main peak at the oscillation frequency ω_0 is smaller. This results in a better frequency stability for L_{12} compared to L_{11}, as will be later discussed in Section 3.4.5.

3.4.4 Power consumption

The bias current I_{DD} provided to each circuit by the power supply was measured using a source meter. The supply voltage V_{DD} being set at 10 V, the power consumption P can be calculated as such

$$P = I_{DD}V_{DD}. \tag{3.45}$$

The power consumption of each oscillator is presented in Table 3.3. There are no major differences in the power consumption between each circuit, meaning that the inductor does not have much influence on this parameter.

For this design, V_{DD} is set at 10 V, but can easily be reduced to 5 V to both decrease power consumption and make it possible to supply it with the same power supply as a microcontroller, which usually is at 5 V. The main power consumption comes from the amplifier circuit, the power dissipated by the series resistance of the inductors is several orders of magnitude smaller than the resistances used to bias the transistor, which explains why it does not have any influence on the power consumption.

	L_{11}	L_{12}	L_{21}	L_{22}	L_{32}
Power consumption [mW]	36.49	36.2	33.14	36.84	37.36

Table 3.3: *Power consumption of each oscillator*

3.4.5 Measurement of the frequency stability

Frequency counting

To measure the frequency of the oscillator, the oscillator is interfaced with a microcontroller Teensy 4.0 that has a 600-MHz clock processor, acting like a frequency counter. This microcontroller takes a square clock signal between 0 and 5V as input, and outputs the frequency of this signal. It can count the frequency of up to ten different signals on ten different pins at the same time. To calculate the frequency, the Teensy counts the number of rising edges, denoted as N, over a certain period of time ΔT. The frequency can then be computed as

$$f = \frac{N}{\Delta T}. \tag{3.46}$$

As the input clock signal might not be perfectly synchronized with the counting window, there is an incertitude over the instantaneous value of the frequency for each measurement. The incertitude of this measurement is of ± 1 input cycle count, which means that the incertitude $e(f)$ over the frequency is

$$e(f) = \frac{1}{\Delta T} \tag{3.47}$$

To increase the resolution on the instantaneous frequency, one has to increase the window during which the counter accumulates the cycle count. It is also possible to average out the error by counting the frequency for several time windows in a row and taking the

average of the frequency over this measurement time. This is equivalent to increasing the value of the time window, except that one can get more measurements in the same amount of time, which is more suitable in the context of nanoparticles detection. Indeed, if the counting time window is large, i.e., 10s, one would need to wait for a new time window to start before introducing the sample with nanoparticles so that the frequency of the oscillator does not change in the middle of the counting window.

In this work, the counting time window is set to 1s, which gives an error of 1 Hz for a single window. However, as the frequency is counted for several windows in a row, this error isreduced down to $1/N_{wind}$ Hz, where N_{wind} is the number of windows during which the signal is counted. This is a good trade-off between speed of measurement and frequency resolution. A moving average over five samples on the frequency value is then performed in post-processing, to smooth the frequency signal.

Characterization of the precision of the Teensy

The stability of the frequency counting of the Teensy is characterized by measuring its output measured frequency when a 5-V clock signal generated by a crystal oscillator is connected at its input. The frequency is measured for 40 minutes for the first and second channels, as only these two are used later on in this work. Table 3.4 presents the results obtained for the characterization.

It has to be noted that sometimes, the Teensy outputs a single sample whose value completely deviates from the value of the previous and next samples. As the deviation for these samples was more than 50 Hz, and it only occurred less than five times during the 40 minutes of measurement, these are considered outsiders and they are removed before calculating the mean and standard deviation of the measured frequency.

Channel	Mean frequency [Hz]	Sigma [Hz]
1	32767.995	0.308
2	32767.994	0.276

Table 3.4: *Mean and standard deviation of the frequency measured by the Teensy when the input is a signal from a crystal-based clock. The incertitude on the frequency measurement is then negligible compared to the drift of the oscillators are measured.*

The crystal clock used to perform the characterization was a DS32 oscillating at precisely 32 768 Hz. As expressed by the value in the table, the Teensy does indeed provide a measurement of the frequency with a standard deviation of less than 1 Hz, meaning that its contribution on the frequency variation that can be observed during measurement is minimal.

Conditioning chain to interface the Teensy

Before being connected to the input pin of the Teensy, the oscillator signal must be converted into a clock signal that oscillates between 0 and 5 V. To do this, a small conditioning chain is designed to transform the sinusoidal signal output by the oscillator into a square signal oscillating between 0 and 5 V. This conditioning chain is presented in Figure 3.19, with the corresponding signal output of each block in Figure 3.20. The signal from the oscillator is retrieved through a buffer to avoid disturbing the circuit.

It is then amplified and fed to a comparator to get a square signal. Finally, a CD4050 non-inverting buffer ensures to have a perfectly square signal in the right range for the Teensy.

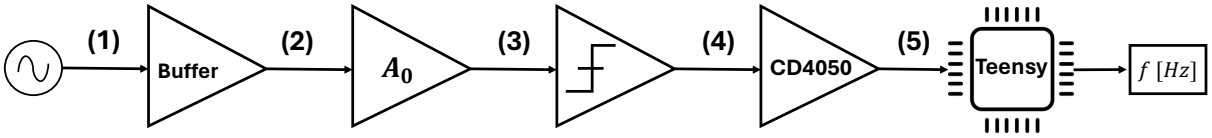

Figure 3.19: *Block schematic of the interfacing chain between the oscillator and the Teensy 4.0. The evolution of the signal at each point of the conditioning chain is presented in Figure 3.20.*

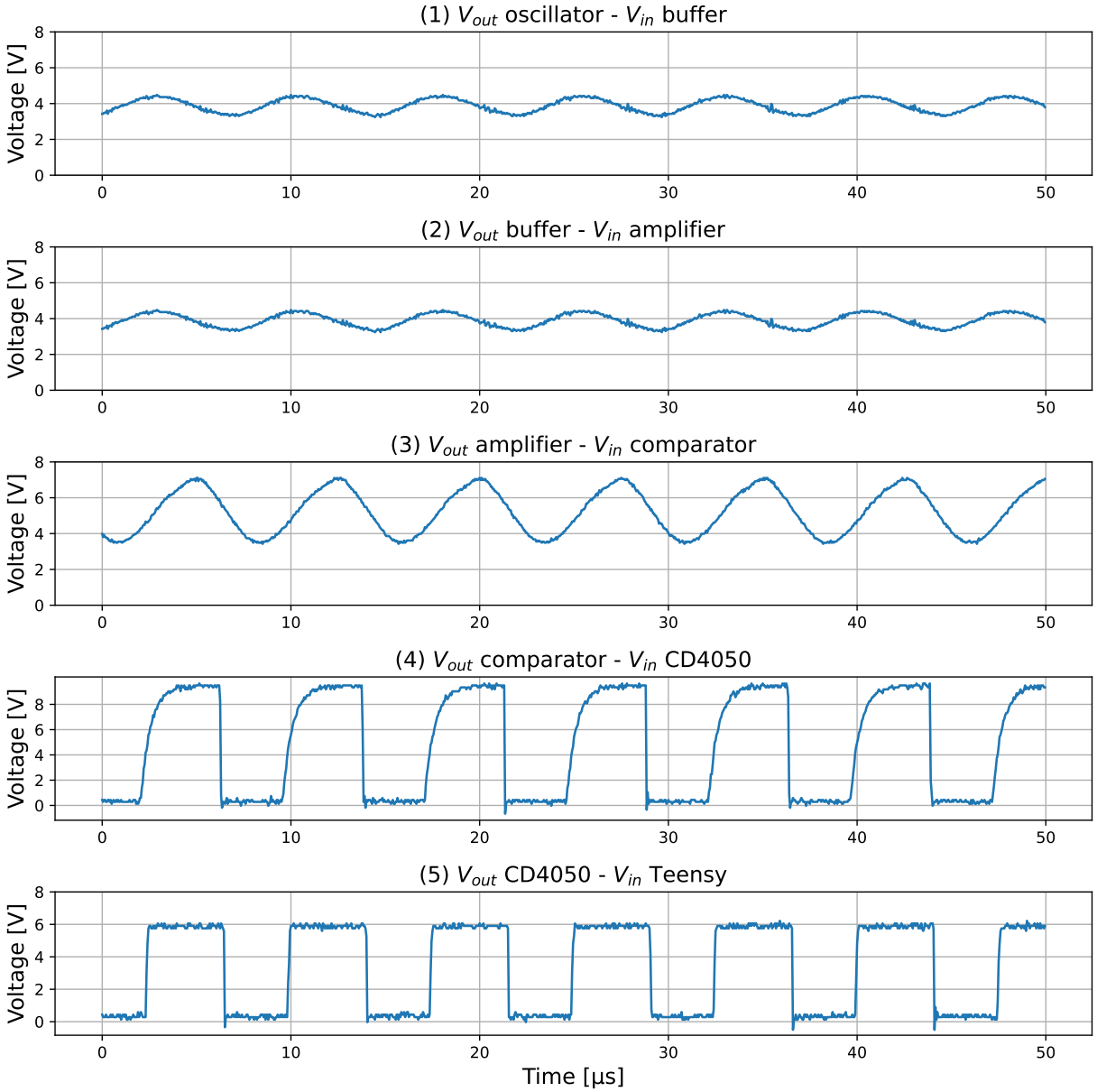

Figure 3.20: *Signals at each point of the conditioning chain presented in Figure 3.19*

.

Frequency stability of the CO

Six COs are soldered on PCB, each with one of the inductors presented in Section 3.4.2. The frequency variation over a one-hour period is measured for each of these oscillators. This enabled us to get an idea of the impact of the inductor on the frequency stability of the signal produced by the oscillator.

Table 3.5 shows the results that were obtained. The theoretical frequency is computed based on the value of the inductance measured with the VNA and the formula of the oscillation frequency of a CO, given by (3.3.1) . The measured frequency is the frequency counted by the Teensy, and the Q factor is the theoretical quality factor of the resonator calculated with the formula derived in Section 3.3.3 and reminded here:

$$Q = \omega_0 \frac{L}{R_L}, \tag{3.48}$$

where ω_0 is the oscillation frequency and R_L is the series resistance of the inductor. The σ/μ is the standard deviation normalized by the mean frequency, and the Δf is the -3 dB resonance width, calculated based on the value of the Q factor and the oscillation frequency.

Inductor	**Th. freq. [Hz]**	**Meas. freq. [Hz]**	σ **[Hz]**	σ/μ **[ppm]**	**Q factor**	Δf **[kHz]**
L_{11}	393 792	388 743	20.68	53	24.5	15.86
L_{12}	401 773	393 225	15.07	38	73.2	5.37
L_{21}	192 539	189 121	4.2	22	24.61	7.68
L_{22}	185 905	176 431	3.46	19	72.5	2.43
L_{31}	135 597	132 900	10.7	80	24.67	5.39
L_{32}	129 965	119 076	5.07	42	53.44	2.22

Table 3.5: *Comparison of the frequency stability of the oscillator with each inductor. σ is the standard deviation of the frequency, and the ratio σ/μ is the standard deviation normalized by the mean frequency of oscillation*

The first thing to observe is that the correspondence between the theoretical frequency and the measured frequency is relatively close. Except for L_{22} and L_{32} where there is an error of 5 and 9%, respectively, the average error between the theory and the measured frequency is less than 2%. This error can come from the fact that the components that were used have a certain tolerance (1% for the capacitors of the resonator), which means that their exact value is not known. It can also come from the fact that some simplifying hypotheses were made when calculating the expression of the oscillation frequency.

Regarding the Q factor of the inductors, it can be observed that, while there is a clear improvement between the inductors with a smaller wire section and the one with a larger one, there is no improvement at all between each pair of inductors. The reason for this is that, while the Q factor depends on the ratio $\frac{L}{R_L}$, it also depends on the frequency of oscillation. The expression of Q can be developed by injecting the expression of the oscillation frequency in its definition:

$$Q = \sqrt{\frac{2}{LC_{res}}} \times \frac{L}{R_L} \tag{3.49}$$

$$= \sqrt{\frac{2}{C}} \times \frac{\sqrt{L}}{R_L}. \tag{3.50}$$

The value of the inductance increases with the square of the number of turns, while the series resistance increases linearly with the number of turns. This means that increasing the number of turns such that the ratio $\frac{L}{R_L}$ increases does not improve the quality factor, as the variation of L and of R_L exactly compensate each other.

Regarding the Q factor of L_{32}, it is equal to 53, which is a bit lower than those of L_{12} and L_{22} (which are at 72 and 73), but its series resistance is also higher than theirs compared to its inductance value. The inductance value of L_{32} is double the inductance of L_{22}, and while its resistance should have been multiplied by 1.3 (as there is only a 1.3 factor between their respective N), it was also multiplied by 1.8, which explains why the Q factor is lower. This could be caused by defects in the wire, or other imperfections that would cause the series resistance to increase.

Finally, while it is important to look at the absolute frequency variation over time, it is also important to put it into perspective with the oscillation frequency. Indeed, a sigma of 10 Hz for an oscillation frequency of 10kHz is not the same than a sigma of 10 Hz for an oscillation frequency of 1MHz. Looking at the values in Table 3.5, there is indeed an improvement between the inductors in each pair, however, there is no clear tendency between pairs.

Figure 3.21 shows the relative frequency variation with respect to the mean frequency over time. It can be observed that the frequency variation takes the form of a slow drift. This means that during a short period of time, i.e., less than five minutes, the frequency is relatively stable, which could lead to a good limit of detection (LoD). However, this will be discussed in more depth in the next section on nanoparticles detection.

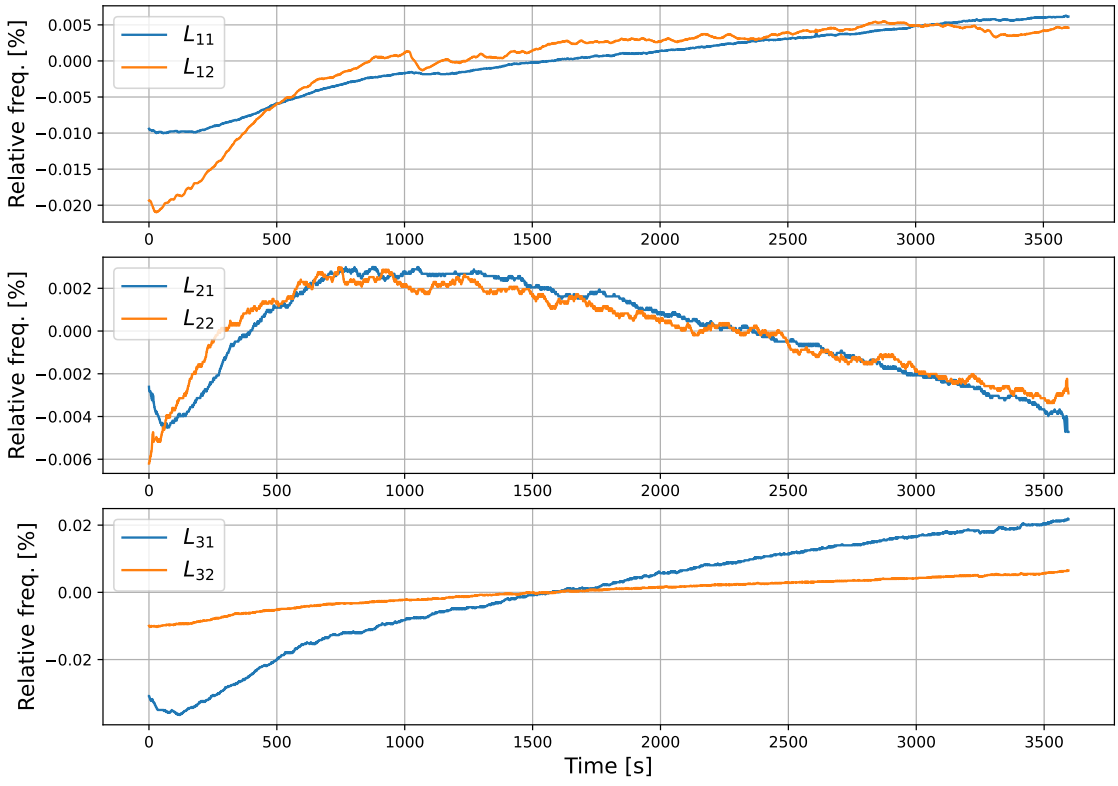

Figure 3.21: *Relative frequency variation [%] with respect to the average oscillation frequency over a 1-hour measurement time. Each pair of oscillator is represented on the same graph.*

It has to be noted that the drift seems to be linked to environmental factors. Indeed, each pair of oscillators is measured at the same time, using the same power supply, and the frequency variation within each pair seems to be correlated. This suggests that this long term drift is not entirely due to internal random noise specific to each individual oscillator, but that some external factor has a similar impact on two oscillators measured in identical conditions. Based on this observation, the idea of a differential system, with two identical oscillators, one serving as a reference and another as the sensing device, could be envisaged to mitigate the effect of the drift on the detection. Another possibility is that the harmonics that can be observed in the signal spectrum in Section 3.4.3, present in the spectrum of the signal are partially responsible for this frequency drift. One would therefore need to find a way to suppress, or a least minimize them. However, this would require further investigation to determine which factor, environmental or the harmonics, has the most influence on the frequency drift.

3.5 Detection and quantification of nanoparticles

3.5.1 Description of the nanoparticles samples

The samples used to characterize the impact of the nanoparticles on the inductance value, and consequently, on the oscillation frequency, are presented in Figure 3.22.

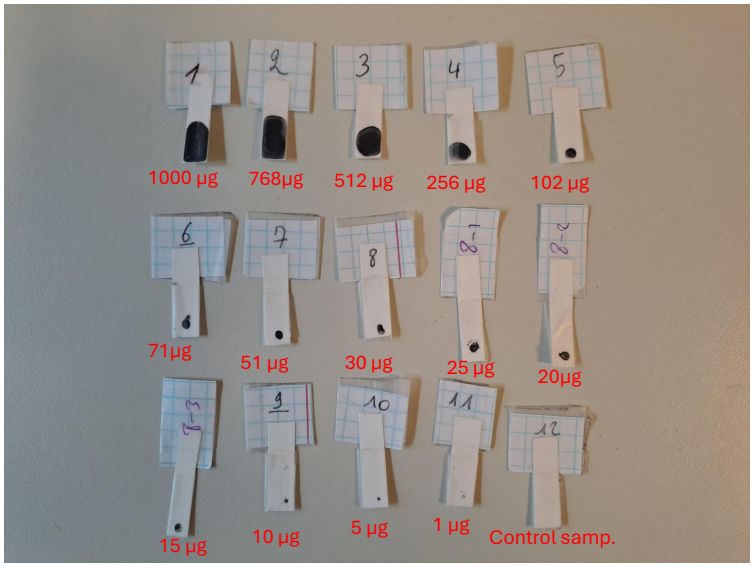

Figure 3.22: *Samples used to characterize the impact of the nanoparticles on the inductance value, and on the frequency variation. The quantity of nanoparticles in these samples ranges from 1 mg and 1 µg, with sample 12 serving as the control sample, without any nanoparticles.*

The mass of nanoparticles ranges from 1 mg down to 1 μg. The sample 12 does not contain any nanoparticles and serves as a control sample to verify that the paper does not have an influence on the inductance value. The mass of nanoparticles in each sample is presented in Table 3.6. The nanoparticles used in this work are commercial iron nanoparticles with an average diameter of 161 nm and a standard deviation on the diameter of 104 nm.

Sample number	Mass of MNP [μg]	Sample number	Mass of MNP [μg]
1	1025	8-1	25
2	768.75	8-2	20
3	512.5	8-3	15
4	256.25	9	10.25
5	102.5	10	5.125
6	71.75	11	1.025
7	51.25	12	0
8	30.75		

Table 3.6: *Samples used to characterize the system*

All tests and characterizations that are presented in the following sections are carried out with these samples.

3.5.2 Definition and characterization of the detection threshold

The way one calculates the detection threshold is key in determining the actual performance achievable with this system. The parameter having the greatest impact on this threshold in this case is the frequency drift caused by the phase noise present in the circuit. Indeed, in such a free-running oscillator, the instantaneous frequency randomly varies around the theoretical oscillation frequency, and the magnitude of this deviation is determined by the characteristics of the oscillator, i.e., its quality factor. However, there is no simple way to link the quality factor to an effective value of the maximum drift an oscillator can have. The discussion that follows is then based on the empirical data collected during the characterization of this system. While this provides a value for the threshold that is only valid in this exact case, the methodology can be translated to other similar systems, enabling a relevant comparison.

A safe approach

One possible way to define the detection threshold is to determine the long-term drift of the oscillator, to calculate its standard deviation σ_{LT} and define the threshold from which a detection is considered as:

$$f_{min} = f_0 \pm 3\sigma_{LT}, \tag{3.51}$$

with f_0 the average oscillation frequency. This definition would make sense if the frequency variations were abrupt, with variations of several Hz over a couple of seconds. However, in steady state, the oscillation frequency of such oscillators varies slowly over time and is relatively constant for a short measurement window, as can be seen in Figure 3.21. Such definition of the detection threshold does not take this parameter into account and does not reflect the real performance achievable with this system.

A conservative approach

A more appropriate way to define the detection threshold would be to try and determine the maximum frequency variation possible during the measurement period, and calculate a threshold from there. This is the approach proposed by [50], where the noise floor is calculated for a given measurement period τ. The advantage of this technique is that it also gives a methodology to determine the duration of the measurement window, provided one

knows the phase noise of the oscillator. In the article, the normalized frequency detection sensitivity within a measurement period τ is expressed as

$$\sigma^2_{\frac{\Delta f}{f_0}}(\tau) = \frac{4}{\pi\omega_0^2\tau^2}\int_0^\infty [S_{\phi,osc}(\omega) + S_{\phi,env}(\omega)]\sin^2\left[\frac{\omega\tau}{2}\right]d\omega \tag{3.52}$$

$$= \frac{1}{\tau^2}\left[\sigma^2_{osc}(\tau) + \sigma^2_{\frac{\Delta Temp}{Temp}}(\tau) + \sigma^2_{\frac{\Delta VDD}{VDD}}(\tau) + \sigma^2_{\frac{\Delta T_{win}}{T_{win}}}(\tau)\right], \tag{3.53}$$

where ω_0 is the average oscillation frequency, ω the offset frequency for the single-sideband phase noise profiles $S_{\phi,osc}(\omega)$ and $S_{\phi,env}(\omega)$, and σ^2 the accumulated jitter due to the intrinsic noise of the oscillator or due to external parameters, i.e., temperature or supply voltage variations. T_{win} corresponds to the variation of the frequency standard of the clock used to count the frequency of the oscillator. As it is commonly generated by high-quality sources such as quartz, its jitter is usually negligible with regards to the other quantities.

Based on this, the graph presented in Figure 3.23 can be obtained, to represent both the phase noise (left) and the impact this phase noise has on the jitter, depending on the window size (right). The detection threshold is then defined as a function of the accumulated jitter during a given window duration, or equivalently, as a function of the frequency drift during this window.

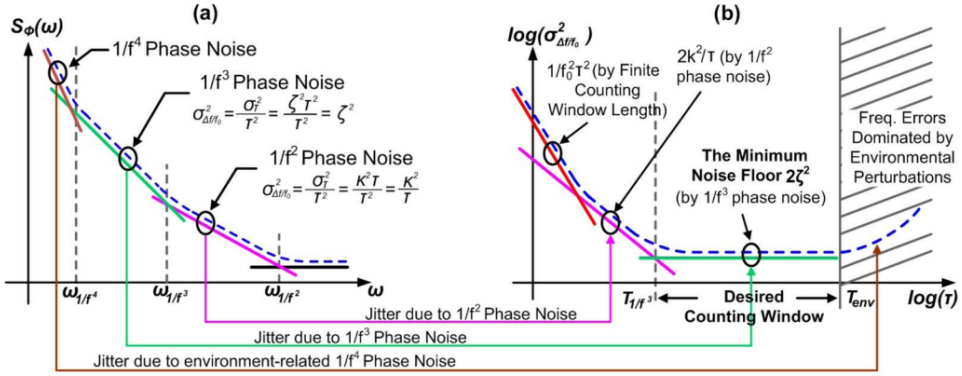

Figure 3.23: *Illustration of the relationship between phase noise and jitter, extracted from [50]. Figure (a) shows the typical phase-noise profile with respect to the offset frequency ω . Figure (b) shows the resulting frequency measurement sensitivity as the total accumulated jitter with respect to the counting window τ.*

To estimate the frequency drift over a small window of time for the different oscillators that were built, an operation similar to a moving average was performed on a measurement of the frequency over a 1-hour period. The only difference is that instead of calculating the average, we calculated the standard deviation. This thus becomes a so-called moving sigma. Figure 3.24 shows the result of this operation, where the window length is 90 s. The justification for this duration will be detailed in Section 3.5.4 relative to the measurement of the frequency variation caused by nanoparticles, but fundamentally, it is related to the discussion summarized in Figure 3.23.

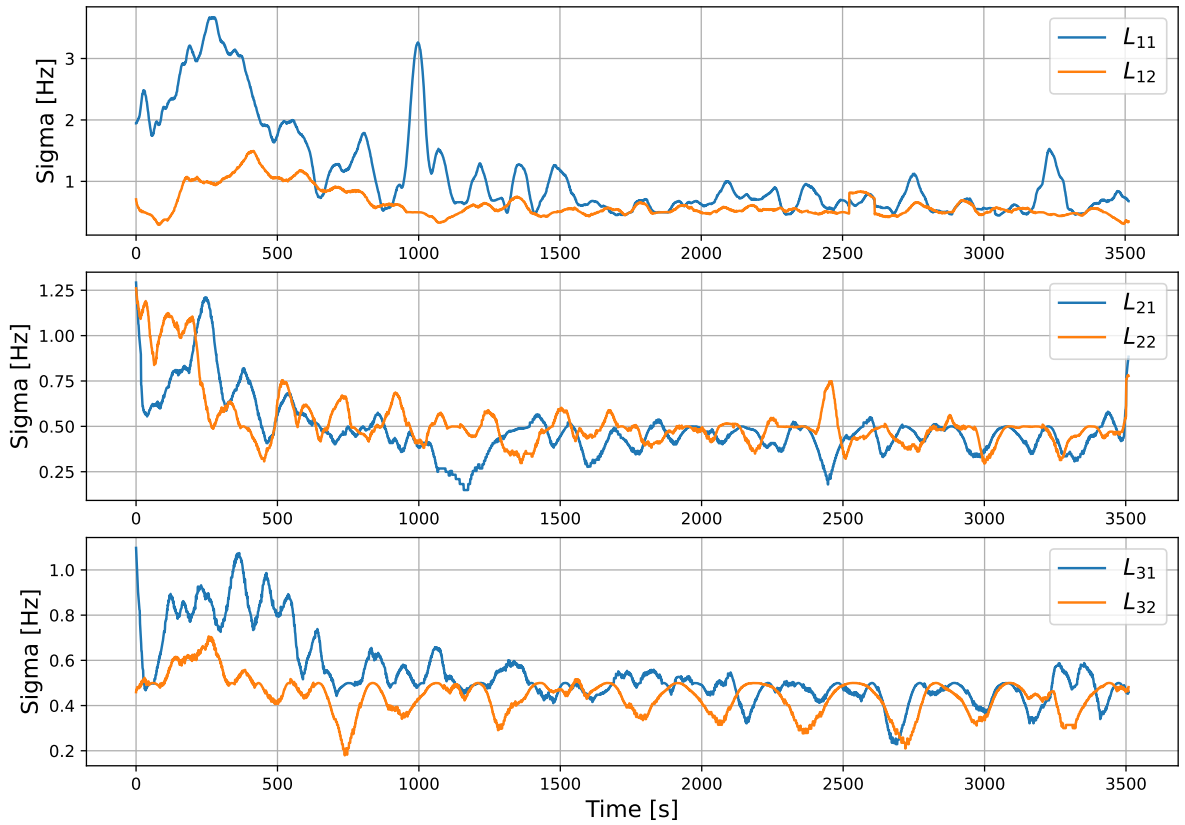

Figure 3.24: *Moving sigma calculated for a 1-hour frequency measurement. The moving window on which the sigma was calculated has a length of 90 s, with one frequency measurement taken every second.*

Table 3.7 shows a comparison between the different definitions of the threshold, and it is clear that the standard deviation of the short-term drift σ_{ST} is much smaller than that of the long-term drift σ_{LT} of the oscillators. The detection threshold f_{min} using the short-term sigma then becomes:

$$f_{min} = f_0 \pm 3\sigma_{ST,max} \tag{3.54}$$

where f_0 is the average frequency during the measurement period and $\sigma_{ST,max}$ is the maximum standard deviation that is observed over the measurement period. This definition better reflects the fact that the measurement time of this system is relatively short.

Ind.	f_0 [Hz]	σ_{LT} [Hz]	$3\sigma_{LT}$[Hz]	$\frac{3\sigma_{LT}}{f_0}$ [ppm]	$\sigma_{ST,max}$ [Hz]	$3\sigma_{ST,max}$ [Hz]	$\frac{3\sigma_{ST,max}}{f_0}$[ppm]
L_{11}	388 743	20.68	62.04	159	3.67	11.01	28
L_{12}	393 225	15.07	45.21	115	3.58	10.76	27
L_{21}	189 121	4.2	12.6	66	1.29	3.87	20
L_{22}	176 431	3.46	10.36	58	1.26	3.78	21
L_{31}	132 900	10.7	32.21	242	1.09	3.29	8
L_{32}	119 076	5.07	15.21	127	0.7	2.11	6

Table 3.7: *Comparison of the two definitions of the detection threshold, with the standard deviation, the minimum frequency variation needed to consider a detection and the normalized frequency variation*

A performance-oriented approach

However, as can be observed in Figure 3.24, the standard deviation over a short-time measurement period is not constant. This means that if the standard deviation of the frequency during the measurement can be estimated, it can lead to a better detection, as the detection threshold adapts itself depending on the measurement conditions at a given moment. Its definition is then be the same as the conservative one, except that the sigma is the one during the given measurement period.

While this definition is a bit more dependent on the measurement conditions at a given instant, it gives an idea of the performance reachable with this detection technique, and what can be achieved if the oscillator that is used has a more stable frequency. This definition of the threshold is compared to the conservative definition in Section 3.5.4, and the performance reached with it are indeed better.

3.5.3 Inductance variation due to magnetic nanoparticles

The inductance depends, among other things, on the magnetic permeability of its core. Introducing nanoparticles inside a coil changes the magnetic permeability of its core, thus changing the value of its self-inductance. To determine the impact of the nanoparticles on the inductance value of the coils used in this work, their inductance is measured with an impedance analyzer when nanoparticles are inserted inside. Figures 3.25a and 3.25b depict the inductance variation with respect to the mass of nanoparticles. The relative variation was calculated as

$$\text{Relative Variation} = \frac{L_{MNP} - L_0}{L_0} \times 100 \tag{3.55}$$

where L_{MNP} is the inductance value with nanoparticles, and L_0 the inductance value without nanoparticles. It can be noted that the mass of nanoparticle in linear scale in Figure 3.25a, to highlight the relationship between the mass of nanoparticles, while it is in logarithmic scale in Figure 3.25b to have a better grasp on the inductance variations for smaller quantities of MNP.

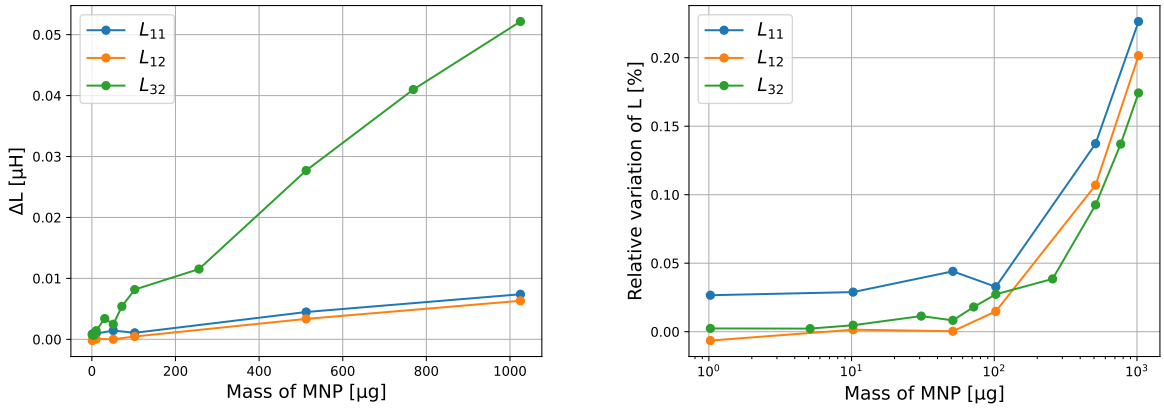

(a) ***Absolute variation of L*** *with respect to the mass of MNP - Mass in* ***linear*** *scale*

(b) ***Relative variation of L*** *with respect to the mass of MNP - Mass in* ***logarithmic*** *scale*

Figure 3.25: *Inductance variation due to nanoparticles*

First of all, Figure 3.25a shows a linear relationship between the inductance variation and the quantity of nanoparticles, confirming a result from [24]. Secondly, while the absolute

inductance variation is much bigger for the L_{32} inductor than for L_{11} and L_{12}, its relative variation is smaller. One hypothesis than could explain this is the fact that in order to obtain a larger inductance for L_{32}, the number of turns to reach this inductance value is three times bigger than for L_{11}/L_{12}. This means that L_{32} has more layers of wire wound on top of each other, resulting in a coil having a higher effective cross-sectional area. If the cross section area of the coil is bigger, the volume of its core is higher, hence the relative volume of the core occupied by a given mass of nanoparticles is smaller compared to a coil with less turns, and a smaller core volume. The relative impact of the nanoparticles on the inductance value is then smaller. The same is true between L_{11} and L_{12}. The wire used to would L_{12} is twice bigger in diameter, and while L_{11} only required one layer of turn to reach 30 turns, L_{12} needed two, thereby increasing its effective cross-section area. This hypothesis should be confirmed by more extensive testing, but this could be a way to improve the sensitivity of this sensor, by trying to find the optimal inductor design to maximize the detection, probably by minimizing as much as possible the core volume.

3.5.4 Oscillation frequency variation due to magnetic nanoparticles

Theoretical impact

As the nanoparticles affect the value of the inductance, they therefore impact the oscillation frequency. Let ΔL be the absolute variation of inductance caused by nanoparticles and L_0 the inductance without MNP. The total inductance L_{MNP} then becomes

$$L_{MNP} = L_0 + \Delta L. \tag{3.56}$$

The expression of the oscillation pulsation with nanoparticles ω_{MNP} can then be expressed as a function of the oscillation frequency without nanoparticles ω_0 and the relative inductance variation $\frac{\Delta L}{L_0}$. Injecting this into the expression of the frequency for a CO leads to

$$\omega_{MNP} = \sqrt{\frac{2}{(L_0 + \Delta L)C}} \tag{3.57}$$

$$= \omega_0 \times \frac{1}{\sqrt{1 + \frac{\Delta L}{L_0}}} \tag{3.58}$$

Measurement method and determination of key parameters

The methodology that used to measure the samples is as follows:

- Measure the frequency for 30 s **without** sample to get a mean frequency $f_{0,1}$ over the measurement time
- Measure the frequency for 30 s **with** a sample to get a mean frequency f_1 over the measurement time
- Measure the frequency for 30 s **without** sample to get a mean frequency $f_{0,2}$ over the measurement time

The Δf caused by the sample is then measured as

$$\Delta f = f_0 - f_s \tag{3.59}$$

where f_0 is calculated as the arithmetic mean of $f_{0,1}$ and $f_{0,2}$. This method enables us to get the best estimation possible of the natural frequency, i.e., the frequency without sample,

during the time the sample is measured, which is essential to calculate an accurate Δf. Essentially, it answers the question : "What would the oscillation frequency of the oscillator have been during the sample measurement if nanoparticles had not been introduced into its inductor ?". Estimating the natural frequency in this way accounts for the drift in the frequency of oscillation. If the frequency with the sample is only compared to the value of the frequency before (or after) the sample is introduced, it would make it more difficult to discern whether the observed change in frequency is solely due to the nanoparticles or if it is also influenced by drift.

Regarding the choice for the duration of the measurement window, there are several parameters to take into account. Figure 3.23 summarizes quite well the different parameters that have to be taken into account in the choice of the measurement window.
On one side, this window has to be long enough so that it averages out the error due to the desynchronization between the start of the counting window and the rising edge of the measured signal. As a reminder, the error $e(f)$, expressed in Hz, can be calculated as

$$e(f) = \frac{1}{\Delta T} \tag{3.60}$$

with ΔT the measurement time. It also has to be long enough so that it is beyond the $1/f^3$ corner. On the other side, we want the measurement time to be as short as possible so that the frequency is almost constant during the measurement, therefore minimizing the impact of the drift and of the perturbation due to the environment (temperature changes, power supply variation, etc). A longer window also means that the estimation of the natural frequency f_0 during the sample measurement is less accurate, leading to more variation in the measurements. We have settled for a counting window of 30 s, giving an error $e(f)$ of less that 0.04 Hz on the value of the frequency over the window. Taking a shorter window is possible, but one still has to take into account the fact that introducing the sample in the inductor and letting the system settle takes a couple of seconds, thereby reducing the effective measurement time.

Measurement results

Figure 3.26 shows the frequency variation when nanoparticles are inserted in the inductor. The mass of nanoparticle in Figure 3.26a is in linear scale to highlight the relationship between the frequency variation and the mass of nanoparticles, while it is in logarithmic scale in Figure 3.26b, to have a better view of the variation for smaller quantities of MNP. The measurement procedure was the following:

1. Let the oscillator run for 30 seconds without sample
2. Introduce a sample in the inductor and leave it for 30 seconds
3. Take the sample out, and wait another 30 second before introducing the next sample

The samples are introduced in decreasing order with respect to the mass of nanoparticles they hold. This measurement procedure is repeated four times for each oscillator, meaning that each sample is measured four times by each circuit. The points in Figures 3.26a and 3.26b are the average Δf over the four measurements.

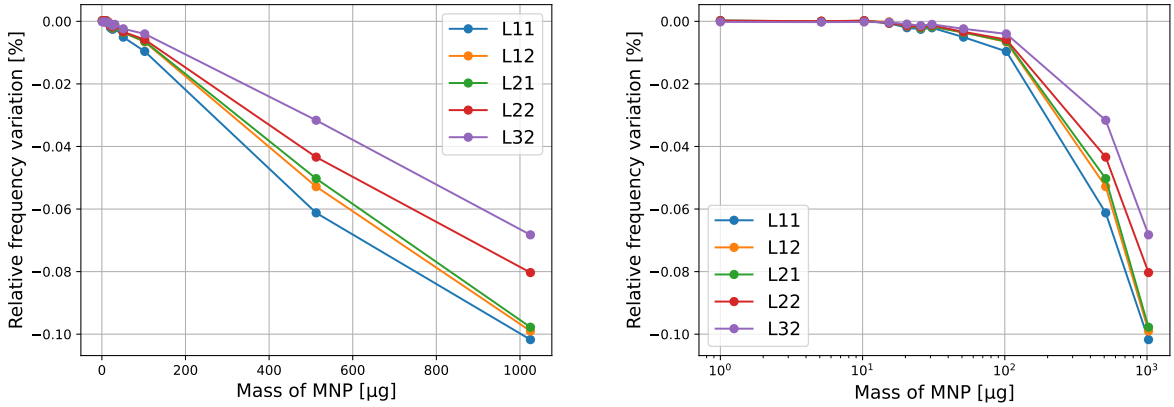

(a) *Frequency variation with respect to the mass of MNP - Mass in* ***linear*** *scale*

(b) *Frequency variation with respect to the mass of MNP - Mass in* ***logarithmic*** *scale*

Figure 3.26: *Frequency variation due to nanoparticles*

The standard deviation of the measurements presented hereabove is displayed in Figure 3.27. It shows that the variability in between two measurements is really small. This is encouraging as it means that this technique could be really adapted to quantify nanoparticles, as the same amount of MNP causes the same frequency variation for different measurements.

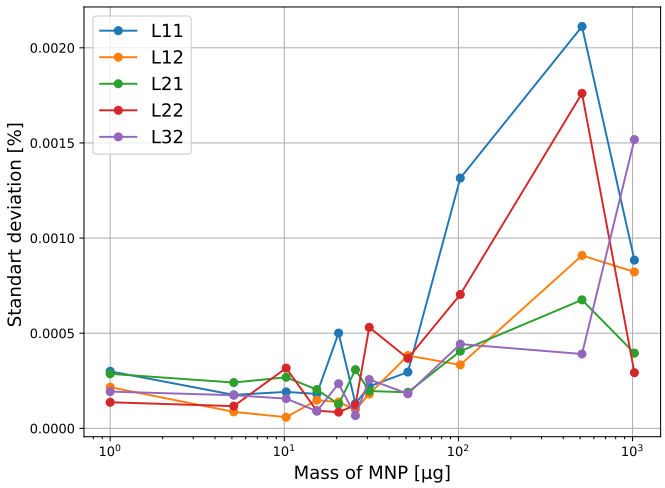

Figure 3.27: *Standard deviation of the measurement presented in Figures 3.26a and 3.26b.*

The relation between the frequency variation and the mass of nanoparticles is linear, as demonstrated in Figure 3.26a, which bodes very well for the development of a sensor able to quantify the nanoparticles on a sample.

As the frequency variation depends on the relative variation of L, the same phenomenon that was observed in the relative inductance variation can be observed in the frequency variation. The relative frequency variation due to the nanoparticles is more important for the smaller inductors than for the bigger one. Moreover, the oscillators with the smallest inductors have a greater oscillation frequency, which means that the same relative inductance variation causes a greater absolute frequency variation than for bigger inductance. This is highlighted in Table 3.8, where it can clearly be observed that the small inductors have a bigger sensitivity than the bigger ones.

	L_{11}	L_{12}	L_{21}	L_{22}	L_{32}
Sensitivity [Hz/µg]	0.395	0.393	0.185	0.142	0.082
σ [Hz/µg]	0.0048	0.0048	0.001	0.0035	

Table 3.8: *Sensitivity of the oscillators, in Hz/µg. The smaller the inductor in the oscillator is, the greater the sensitivity is.*

Comparison between theoretical and measured frequency variations

With the measurements that are carried out, it is possible to validate whether the expression 3.5.4 that predicts the frequency variation with respect to ΔL is accurate. To do this, the theoretical frequency variation is calculated using (3.5.4), using the inductance variations measured with the VNA to determine ΔL. Figure 3.28 shows the results obtained for L_{11}, L_{12} and L_{32}. Measurement noise aside, the theory fits closely to the measured value.

As the ΔL used to predict the theoretical variation comes from a measurement, this introduces a first source of variation. Then there is another source of noise with regard to the accuracy of the Δf. Both the drift and the fact that the value of the natural frequency f_0 to which the frequency with the sample is compared is an estimation and not an exact value, introduce more uncertainty as to what exact Δf is observed.

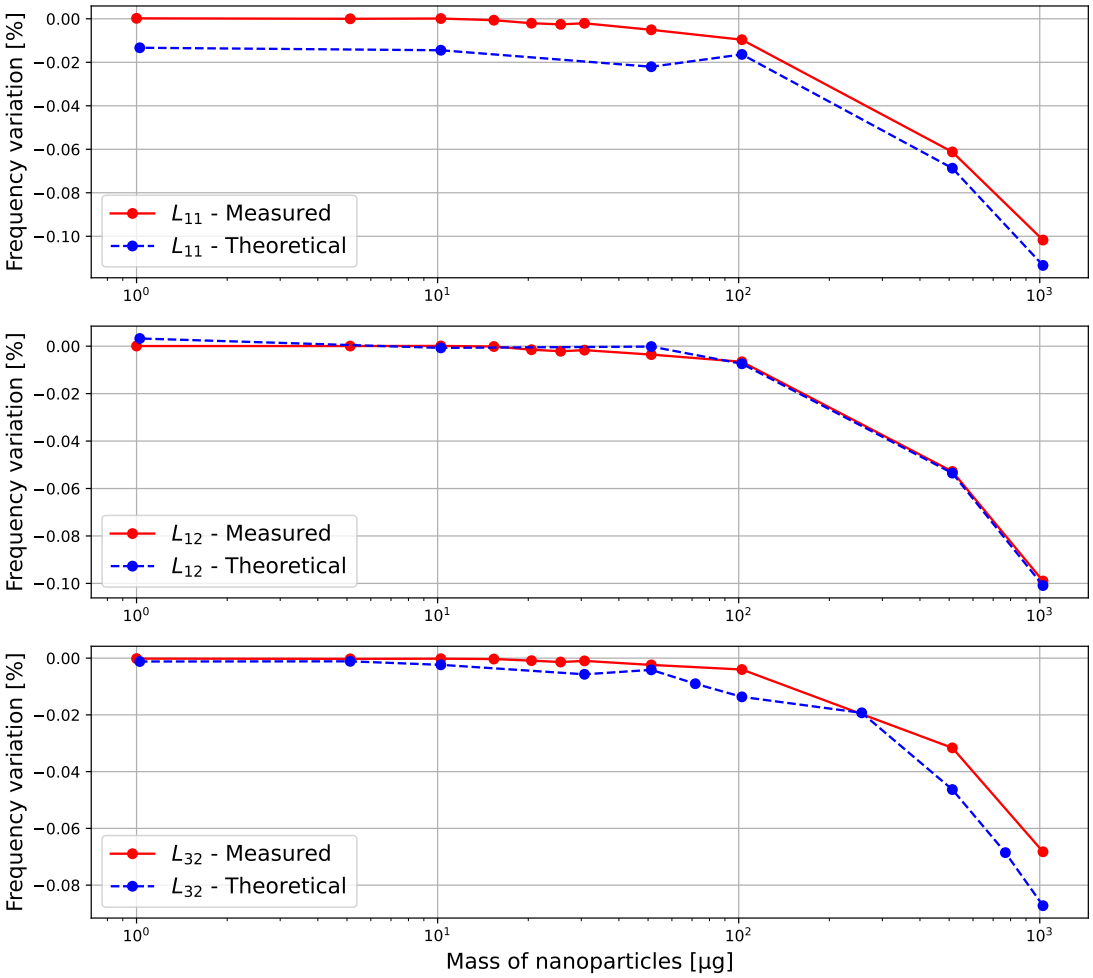

Figure 3.28: *Comparison between the theoretical frequency variation based on the measured inductance variation, and the measured frequency variation - From top to bottom : L_{11}, L_{12}, and L_{32}*

Discussion on the detection threshold

As was hinted before in Section 3.5.2, the performance of the system greatly depends on the way the detection threshold is defined.
The first definition that is proposed is a fixed threshold (FT) calculated based on the maximum drift that is observed over a time window whose length is equal to the duration of the measurement window. The frequency of the oscillator is measured for one hour straight, and the computation of the maximum drift is based on this measurement. This fixed threshold is the same no matter the circumstances, and if at one point the drift during a measurement is lower or higher than this maximum drift, the real performance of the system is not be properly captured by this worst-case definition.

The second definition that is proposed is based on an estimation of the drift during the measurement, to compute an adaptive threshold (AT). To this end, the natural frequency is measured before and after introducing the sample, and the drift is calculated based on these two measurements. This is under the hypothesis that the standard deviation of the drift does not vary substantially during the measurement window. However, as each measurement of the frequency (before introducing the sample, with the sample, and after) is relatively short, the overall measurement time is also short, which makes this hypothesis reasonable. This definition has two advantages. The first one is that, as the detection threshold is calculated on the spot, there is no calibration to do beforehand, to manually enter the value of the fixed threshold in the system. The second advantage is that this enables to adapt the detection to the measurement conditions. If for some reasons, the oscillator is particularly stable during the time a measurement is taken, its actual threshold is much lower and it could detect much smaller quantities of nanoparticles. On the contrary, if the environment in which the measurement is taken is very noisy, i.e., a lot of magnetic noise, a high temperature, etc, this would impact the frequency drift of the oscillator. Having an adaptive threshold enables to take this into account and ensure that there are no false positives.

Figure 3.29 illustrates the difference between the two definitions of the threshold, for two of the oscillators L_{11} and L_{22}, with the hard threshold in dashed green and the adaptive threshold in dashed red. The fixed threshold (FT) is calculated as

$$FT = \omega_0 \pm 3\sigma_{max} \tag{3.61}$$

with σ_{max} the standard deviation of the maximum drift over a 90-s time window observed during the characterization of the oscillator, and ω_0 the natural frequency calculated during the measurement time. The adaptive threshold (AT) has the same definition, except that the standard deviation σ_{adapt} is calculated differently. It is the standard deviation of the drift observed during the measurement window.

$$AT = \omega_0 \pm 3\sigma_{adapt} \tag{3.62}$$

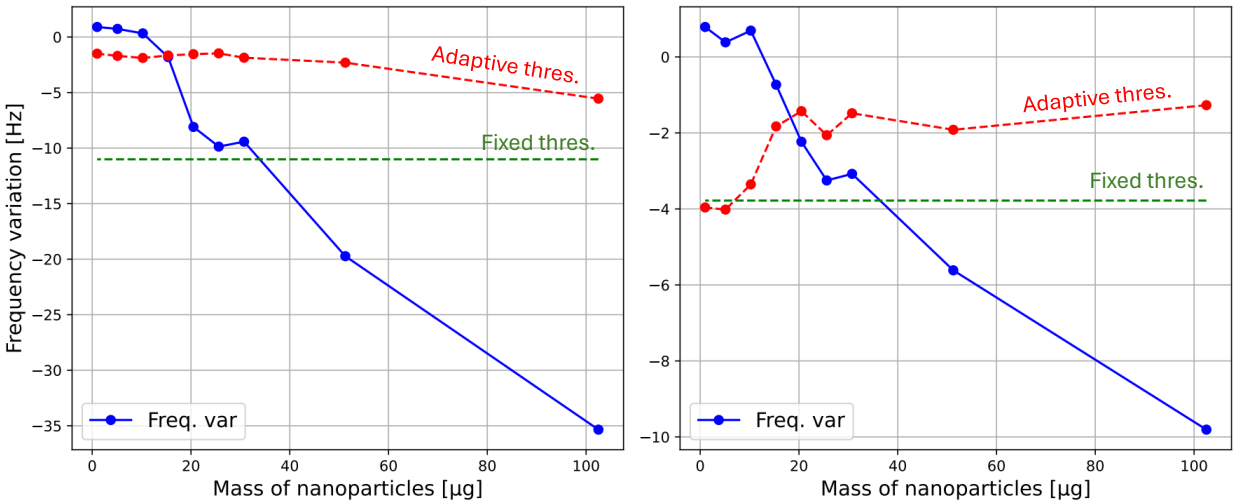

Figure 3.29: *Comparison between the LoD obtained with the adaptive and the fixed detection threshold, for L_{11} (left) and L_{22} (right).*

The two figures are based on a single measurement each, as the adaptive threshold only makes sense in this context. The graph on the left in Figure 3.29 is a good example where the fixed threshold underestimates the real frequency variation detectable by the system at that particular moment. During that measurement, the oscillation frequency of the oscillator is very stable, enabling for a much better detection. The graph on the right in Figure 3.29 on the other hand illustrates that at times, the oscillation frequency can become relatively unstable. During the measurement of the smaller quantities of nanoparticles, the oscillation is quite unstable, and the soft threshold is equal, if not greater than the fixed one. This shows how having an adaptive threshold enables to really take into account the measurement conditions.

As a side note, each point on the graph corresponds to the measurement of one sample. One can notice that one of the point (for 30µg) consistently breaks the linearity of the relationship between the frequency variation and the mass of nanoparticles, by causing a smaller Δf that its predecessor. This means that the actual mass of nanoparticles on this sample is lower that what it is supposed to be. The fact that the system can detect such variation is encouraging towards the development of a system able non only to detect, but also to quantify nanoparticles on a given sample.

Table 3.9 shows a comparison between the limits of detection attainable with each definition. The worst and best case are shown. Regarding the limit of detection attainable with the fixed threshold, there usually is little variation between the worst and the best case. This variation mostly comes from the incertitude on the Δf caused by the drift. If there was a lot of drift during the measurement period, the estimation of the natural frequency to which the frequency with the sample is compared to, is less accurate, leading to more incertitude, hence a worst limit of detection. The variation between the worst and best case is much greater when using the adaptive threshold to determine the limit of detection. While the worst case usually is around the limit of detection given by the hard threshold, the best case often leads to a much better detection, if the drift at the moment of the measurement is lower.

Inductor's name	FT- best	FT - worst	AT - best	AT - worst
L_{11}	25 µg	30 µg	**15 µg**	20 µg
L_{12}	40 µg	40 µg	25 µg	45 µg
L_{21}	25 µg	25 µg	20 µg	25 µg
L_{22}	25 µg	40 µg	20 µg	40 µg
L_{32}	40 µg	45 µg	25 µg	60 µg

Table 3.9: *Limit of detection reached depending on the threshold definition*

The smallest amount of nanoparticles that was detected overall is 15 µg. In the context of Lateral Flow Assay, one of the limiting factor for the quantity of nanoparticles is the size of the test line, and thus the quantity of nanoparticles it can hold. Considering a test line volume between 0.01 and 0.5 mm^3, and a volume occupied by the nanoparticles between 10% and 50% of the total volume, this gives an estimate for the quantity of nanoparticles that we have to be able to detect between 0.1 µg and 50 µg. However, bringing this LoD lower enables to detect for even smaller concentration of bacteria with the LFA. The robustness and the repeatability of this system should also be improved, so that the worst-case LoD is closer to the best-case.

However, this should not be impossible to do. There is a lot of room for improvement, both on the design of the inductor and on the architecture of the oscillator, to make it more stable, frequency wise. Table 3.10 gathers the performance reached in other articles for the detection of nanoparticles in the context of LFA, to compare it with the results obtained in this work. While the more advanced methods, such as the frequency mixing technique or the GMR sensors, can detect nanoparticles in the ng range, the techniques measuring a frequency variation in a system using coils or measuring the variation in the impedance of a coil have a LoD much closer to the one obtained in this work. However, apart from [18], all the other techniques use either microfabrication at some point or necessitate laboratory equipment to carry out the measurement. [18] measures the frequency variation in a VCO controlled by a PLL and actually has a design very similar to us regarding the size of the inductor. Their system is more complex that ours, but it is encouraging as to the LoD reachable using frequency measurements.

Reference	Technique used	Transducer	LoD
[16]	Frequency mixing	Pickup + excitation coils	0.4 ng
[14]	Frequency mixing	Pickup + excitation coils	3 ng
[20]	Wheatstone bridge	GMR	64 ng
[19]	Frequency mixing	Pickup + excitation coils	120 ng/ml
[22]	Wheatstone bridge	GMR	0.84 µg
[22]	Wheatstone bridge	GMR	0.84 µg
[51]	Impedance meas.	Inductor	$\approx$ 1 µg
[51]	Impedance meas.	Inductor	$\approx$ 1 µg
[21]	Wheatstone bridge	GMR	1.2 µg
[18]	Frequency var. meas. in VCO	Inductor	1.2 µg
[17]	Self-frequency var. meas.	Inductor	10 µg
This work	**Frequency var. in LC-oscillator**	**Inductor**	**15 µg**

Table 3.10: *Comparison between the performance of this work and the performance reach in other articles in the context of nanoparticle detection for LFA.*

3.5.5 Possible improvements

There are several improvements possible, both to lower the LoD and to make the system more robust and reliable by bridging the gap between the best an worst case LoD.

Design of the coils

The first thing on can do to improve the limit of detection is optimize the design of the coils. Indeed, as shown in Table 3.8, changing the size of the inductors has a big influence on the detection, as the same amount of nanoparticles does not cause the same inductance variation depending on the inductor's size. Fundamentally, to maximize the detection, one has to minimize the volume of the core of the inductor as much as possible. By doing this, the nanoparticles occupy a much greater portion of the core volume, thereby causing a greater inductance variation. Currently, an elliptic design for the core is used, but it probably is not the best choice. A rectangular core would fit more closely to the shape of the nanoparticles samples and enable for a better detection. Shorter inductors would probably be better too, as ours currently are 10 mm in length, which is long compared to the size of the smaller samples.

Frequency stability improvement

Another possibility to lower the limit of detection is improving the frequency stability of the oscillator. Indeed, the choice is made to define the limit of detection based on the drift that is observed over the measurement time. By designing a more stable oscillator, one can thereby bring the limit of detection down. Clapp oscillators for example are known for their remarkable performance regarding frequency stability[52], having a quality factor up to 10 times better than the quality factor of the CO, with a very similar implementation. The only change in the architecture is the addition of a capacitor in series with the inductor.

Double Differential Frequency Measurement Scheme

Finally, to improve the robustness of the system to frequency drift, one can implement a differential frequency detection [50]. To do this, two identical oscillators are needed, one to generate the reference frequency and the other to detect the nanoparticles. A first Δf_1 can be obtained by measuring the frequency difference between the two oscillators without nanoparticles. The second Δf_2 is obtained by measuring the frequency difference between the two oscillators when nanoparticles are introduced into the sensing oscillator. The frequency shift f_s caused by the nanoparticles can then be calculated as

$$f_s = \Delta f_2 - \Delta f_1 \tag{3.63}$$

The concept of the double differential frequency measurement technique is illustrated in Figure 3.30.

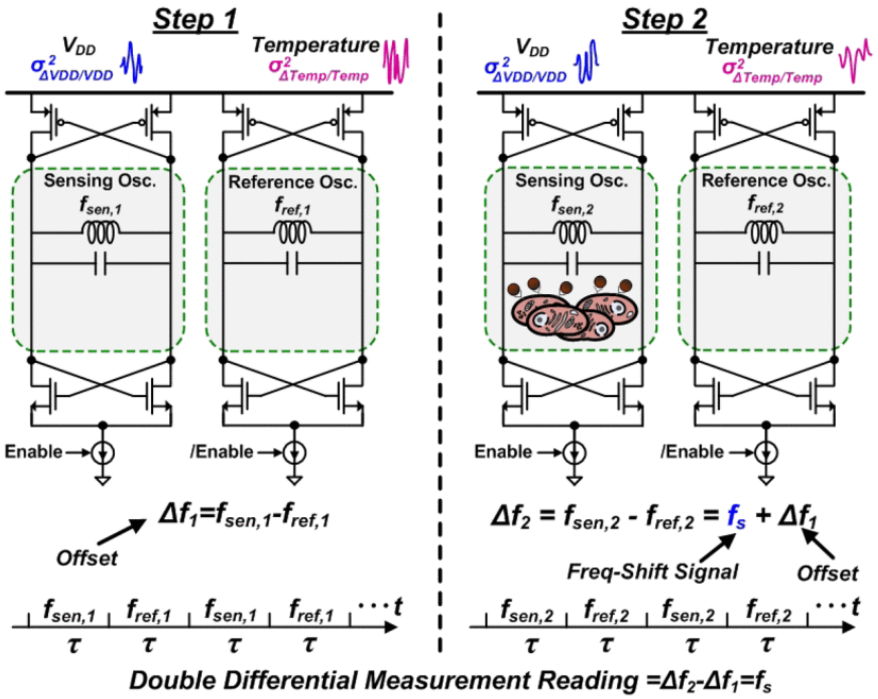

Figure 3.30: *Double differential frequency measurement scheme : working principle. Image from [50]*

Chapter 4

Conclusions and perspectives

The primary objective of this work is to develop a sensor capable of detecting and quantifying magnetic nanoparticles used as labels in the context of LFA. Moreover, this thesis falls within a broader project with the aim of developing a low-cost and portable biosensor to help improve water quality monitoring in regions where resources and equipment are limited. This brings an additional constraint in the design of this sensor, as it has to comply with these cost and portability specifications. However, most of the techniques usually used to detect nanoparticles either require bulky and expensive equipment, or use microfabrication at some point in the production of the magnetic sensor, hence the need of a low-cost, portable sensor. The challenge is then to design a sensor that can both quantify MNP and have a sufficiently low LoD to be useful in the context of LFA, while meeting the additional constraints listed hereabove. It can be estimated that a LFA test zone can contain from 0.1 to 50 µg of MNP, which gives an order of magnitude for the LoD.

To meet the portability and cost constraints, the choice has been made to develop a solution using only off-the-shelf components. Moreover, it has also been decided to work with an inductive sensor, as inductors can easily be fabricated, without requiring anything other than a wire and a support to wound the wire around it. Coil-based sensors also display the broadest range of detection.

A first solution has been attempted, based on the principle of induction. However, several problems arise when trying to implement this solution in practice:

- The perturbation in the induced current caused by nanoparticles is really small, consequently, the voltage variation at the output of the secondary circuit is also really small (< 1 mV). Such a tiny difference is challenging to detect accurately only with off-the-shelf components.
- The system requires a high-frequency excitation signal (in the MHz range) so that the inductors in the system are in their inductive region to maximize induction. Generating such high-frequency signal is not an easy task with basic discrete components.
- The signal generator must be able to provide a high current (several tens to several hundreds of mA) due to the low impedance of the primary circuit. Again, standard drivers are often limited to less than 10 or 20 mA. The signal generator would then require special drivers to work correctly.

All of these challenges make the detection of nanoparticles with this technique not suitable in the context of the development of a low-cost, portable sensor. The decision has

then been made to move on to the other technique, that was the core of this work.

The second technique that has been explored in this work relies on an LC-oscillator whose oscillation frequency depends on the inductance value of the LC network in the oscillator. Several reasons led us to consider this option :

- There exist simple architectures of LC oscillators that can easily be implemented on PCB
- The measurement of the frequency of oscillation can be performed by a microcontroller using a basic frequency counting technique.
- The entire system can be implemented with off-the-shelf components, aligning with the cost and portability requirements.

A Colpitts oscillator has been designed, and several setups with different inductors have been tested to identify the limiting factors of the system and propose ways to improve it. Three pairs of coils have been fabricated. The two inductors inside a pair have the same inductance value but there is about a factor of three between their series resistance R_L. The inductance values across the pairs are 3.1 µH, 13.7 µH and 29 µH, and the lowest R_L R_L of each pair are 0.106 Ω, 0.224 Ω, and 0.412 Ω. To change the R_L of the inductors inside each pair, different wire sections have been used. This means that the inductors with the lowest R_L are also the biggest, as the wire used has a diameter twice bigger than the wire used for the other coils.

It has been observed that the inductors that have the smallest size, i.e., the inductors that have the highest R_L in each pair, are the one showing the best performance regarding nanoparticles detection. The best LoD that has been reached in this system is with the inductor of the first pair with the highest R_L, where 15 µg of nanoparticles have been detected on a paper sample. The sensitivity of this oscillator is 0.395 Hz/µg for an oscillation frequency of 388 kHz. The other inductors have a LoD between 20 and 25 µg. Moreover, a linear relationship between the frequency variation and the mass of nanoparticles has been observed. This facilitates the quantification of MNP on in a sample, and by extension the quantification of bacteria present in water, as their is a linear relationship between the bacteria concentration and the quantity of nanoparticles that are brought to the test zone of the LFA.

Two main improvement points have been identified for this system, that could bring the LoD down, but also ensure the robustness and the repeatability of the measurements.

The first point that needs to be improved is the frequency stability of the oscillator. The threshold at which detection is considered to have occurred is defined as a function of the standard deviation of the frequency observed during the measurement time. For the CO with the inductor having the best LoD, this standard deviation varies from 0.5 to 4 Hz on a 90-s measurement period, depending on the noise level at the moment of measurement. As 15 µg of nanoparticles induce around a 2.5 Hz variation, this shows the importance of have a stable oscillation frequency. To attend this issue, there exist other architectures similar to the CO that have better frequency stability. One can expect an improvement of a factor of 10 in the quality factor Q by using a Clapp oscillator instead of a CO. A double differential frequency measurement scheme could also be envisaged to eliminate the frequency drift due to environmental factors such as temperature or power supply variations.

The second area in which improvement is possible is in the design of the inductors. It has been observed that the bigger the inductor is, the less sensitive it is to the presence of nanoparticles. This is due to the fact that the inductance value of a coil depends on the permeability of its core. If the core of a inductor is small, the nanoparticles occupy a greater proportion of this core, thus having a greatest influence on its permeability. It has been observed that the same amount of nanoparticles caused an inductance variation of 0.225 % for the smallest inductor, and a variation of 0.175 % for the biggest. A further design should then seek to minimize as much as possible the size of the inductor to maximize its sensitivity.

To conclude, what can be remembered from all this ? Firstly, this work has shown that measuring frequency variations in an LC-oscillator is an effective way to detect and quantify small amounts of nanoparticles, while trying to measure voltage variations in a system using induction is not a viable solution in this context. Secondly, the system implementing the frequency counting solution can be build using only off-the-shelf components, which makes it a very attractive solution towards the development of a low-cost and portable sensor. Finally, the LoD reached by this system falls within the useful range for a usage in the context of LFA, and could be brought down even further. This means that, in the broader scope of this project, designing a paper-based LFA biosensor using nanoparticles label is totally possible and relevant, and could prove to be a viable solution in the development of a low-cost and portable sensor destined to monitor water quality in regions where resources and equipment are limited.

Appendix A

Comparison between the full and the simplified transfer function of the general oscillator

Figure A.1 shows the small signal circuit for the open loop analysis, when the biasing base resistors are neglected. Figure A.2 depicts the same circuit, but when the biasing base resistance $R_b = R_{b1}//R_{b2}$ is taken into account.

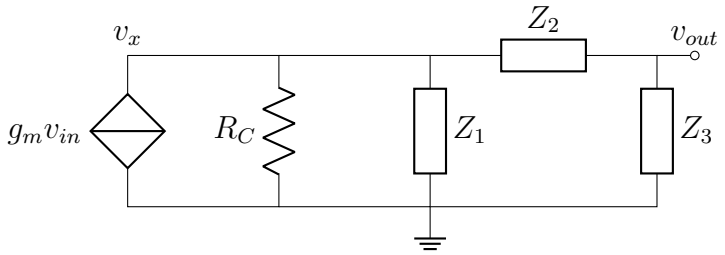

Figure A.1: *Small signal circuit for the oscillator in open loop, neglecting the base resistance* $R_b = R_{b1}//R_{b2}$. C_E *and* C_B *have been replaced by short circuits*

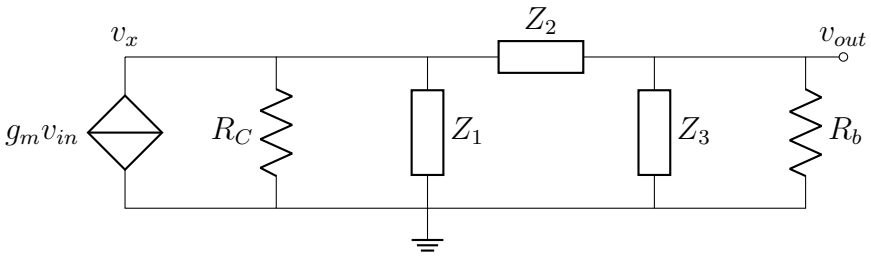

Figure A.2: *Small signal circuit for the oscillator taking the base resistors* $R_b = R_{b1}//R_{b2}$ *into account.* C_E *and* C_B *have been replaced by short circuits*

The transfer function of the circuit in Fig. A.1 was derived in Section 3.2.2.

For the circuit in Fig. A.2, the following equations can be derived by applying the Kirchoff current law at node V_x and V_{out}.

$$\frac{v_{out} - v_x}{Z_2} = \frac{v_x}{Z_1} + \frac{v_x}{R_C} + g_m v_{in}$$
$$\frac{-v_{out}}{R_b} = \frac{v_{out}}{Z_3} + \frac{v_{out} - v_x}{Z_2}$$

By rearranging the two equations to isolate $\frac{v_{out}}{v_{in}}$, the following transfer function is obtained

$$\frac{v_{out}}{v_{in}} = \frac{g_m Z_1 Z_3 R_b R_C}{R_b Z_1 (Z_2 + Z_3) + R_C Z_3 (Z_1 + Z_2) + (Z_1 + Z_2 + Z_3) R_b R_C + Z_1 Z_2 Z_3} \tag{A.1}$$

If the impedances Z are replaced by their corresponding values for the colpitt oscillator, i.e., Z_1 and Z_3 are capacitors and Z_2 is an inductor, one can compute the difference between the result given by the transfer function neglecting the base resistors and the one taking them into account. This difference was calculated for $Z_1 = Z_3 = \frac{1}{j\omega C}$ and $Z_2 = j\omega L$, for C = 100 nF and L = 10 µH. The result is shown in Figure A.3. Except for a small difference at low frequency, the two transfer functions give excatly the same result, confirming that the base resistors can be neglected in the computation of the open loop transfer function.

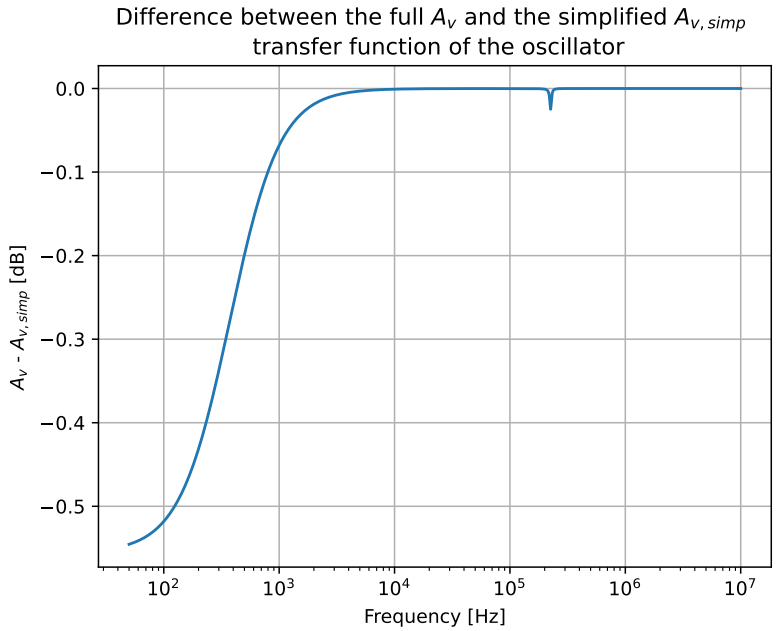

Figure A.3: *Difference between the amplitude given by the colpitts open loop transfer function taking R_b into account and the transfer function neglecting it. There is a small difference at low frequency, but*

Appendix B

PCB

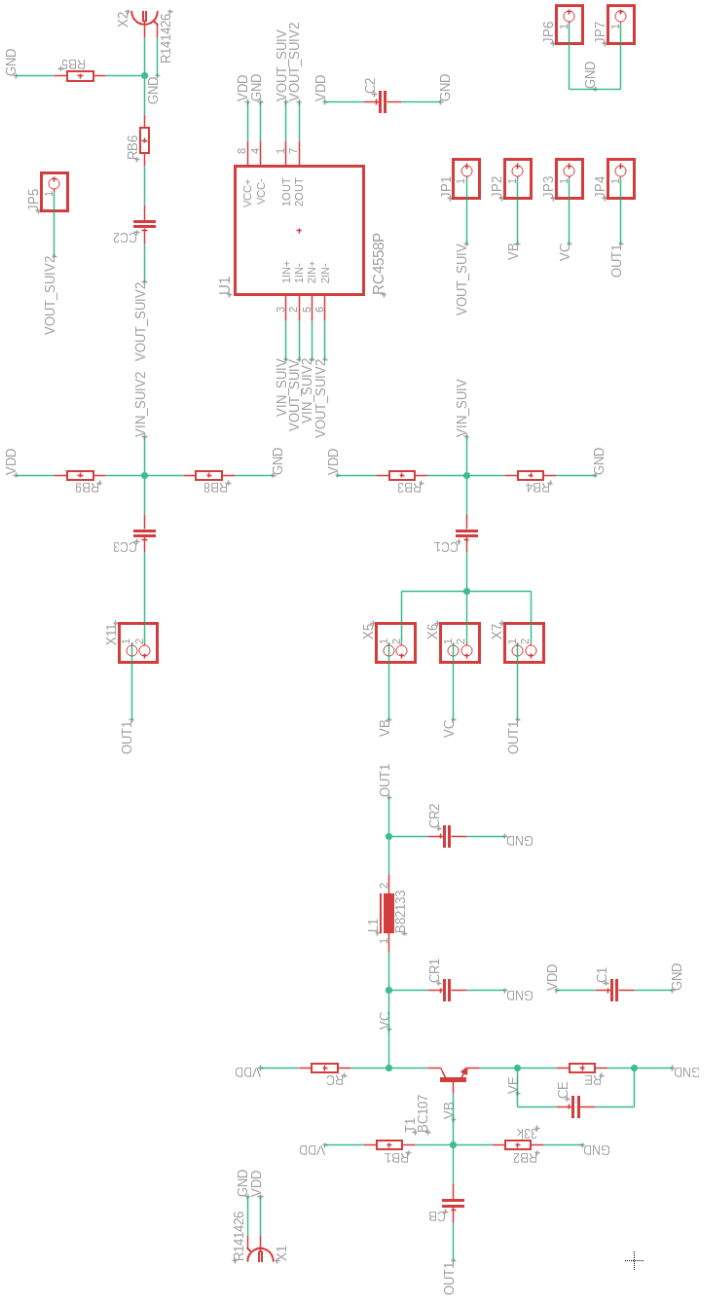

Figure B.1: *PCB schematic of the Colpitt oscillator that was designed*

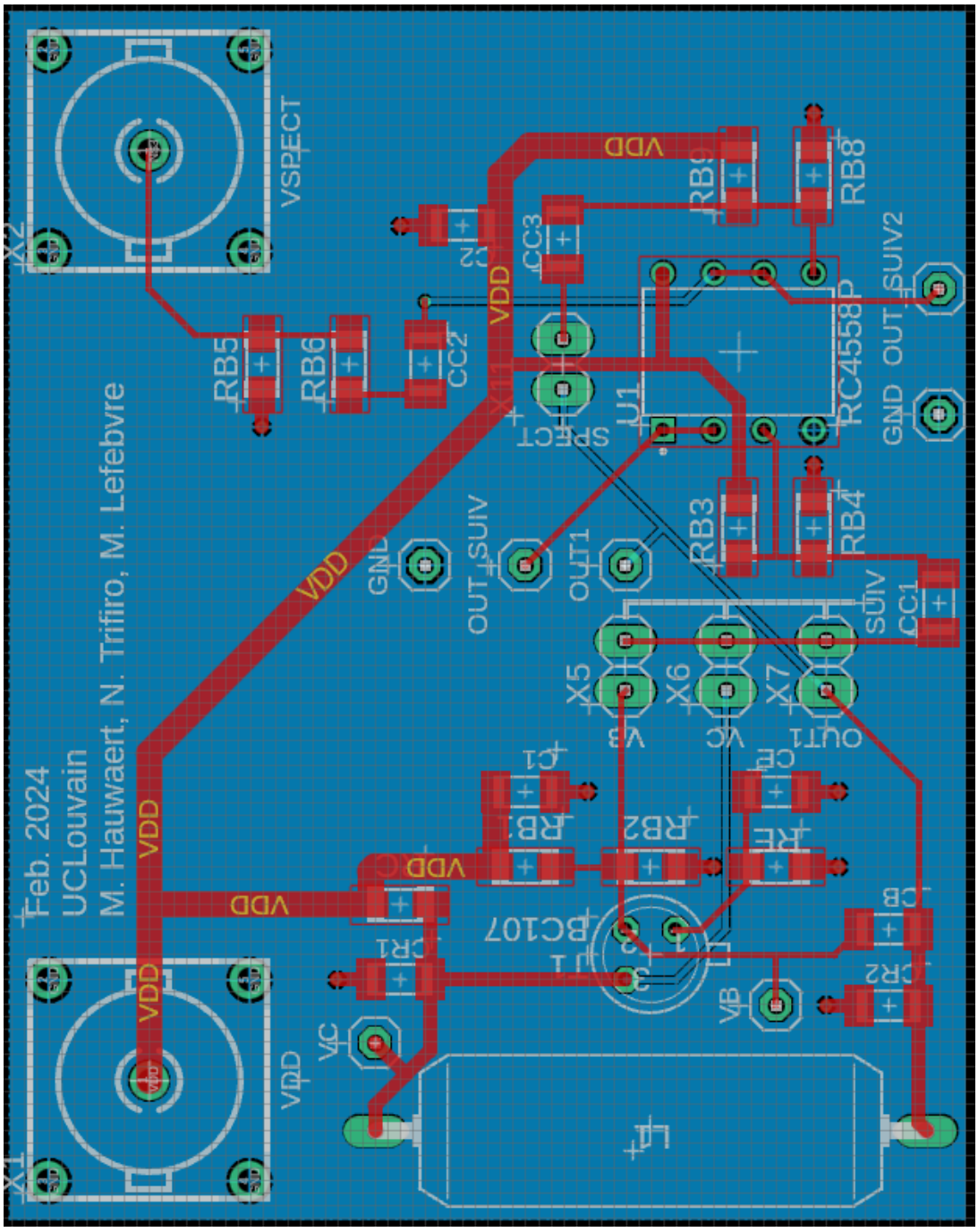

Figure B.2: *PCB board of the Colpitt oscillator that was designed*

Appendix C

Code for frequency counting

C.1 Code for the frequency counting in the Teensy

```
1
2  // Measures 10 frequencies by counting rising edges.  Best for 10kHz to 30
       MHz
3  // Connect frequencies to pins 6, 9, 10, 11, 12, 13, 14, 15, 18, 19
4
5  // https://forum.pjrc.com/threads/71193-Teensy-4-Measuring-multiple-
       frequencies
6
7  // Timer   Pin    Pad ALT input mux
8  // QuadTimer4_1    6    B0_10 1
9  // QuadTimer4_2    9    B0_11 1
10 // QuadTimer1_0   10    B0_00 1
11 // QuadTimer1_2   11    B0_02 1
12 // QuadTimer1_1   12    B0_01 1
13 // QuadTimer2_0   13    B0_03 1 IOMUXC_QTIMER2_TIMER0_SELECT_INPUT=1
14 // QuadTimer3_2   14    AD_B1_02  1 IOMUXC_QTIMER3_TIMER2_SELECT_INPUT=1
15 // QuadTimer3_3   15    AD_B1_03  1 IOMUXC_QTIMER3_TIMER3_SELECT_INPUT=1
16 // QuadTimer3_1   18    AD_B1_01  1 IOMUXC_QTIMER3_TIMER1_SELECT_INPUT=1
17 // QuadTimer3_0   19    AD_B1_00  1 IOMUXC_QTIMER3_TIMER0_SELECT_INPUT=1
18
19 #include <TimeLib.h>
20
21 #define GATE_INTERVAL 1000000  // microseconds for each gate interval
22 #define GATE_ACCUM    1   // number of intervals to accumulate
23 #define MULT_FACTOR   1     // multiply to get Hz output
24
25 typedef struct {
26   IMXRT_TMR_t *timer;
27   int timerchannel;
28   int pin;
29   int pinconfig;
30   volatile uint32_t *inputselectreg;
31   int inputselectval;
32 } timerinfo_t;
33
34 const timerinfo_t timerlist[] = {
35   // Timer     Ch  Pin  Alt Input Select
36   {&IMXRT_TMR4, 1,   6,  1, NULL, 0},
37   {&IMXRT_TMR4, 2,   9,  1, NULL, 0},
38   {&IMXRT_TMR1, 0,  10,  1, NULL, 0},
39   {&IMXRT_TMR1, 2,  11,  1, NULL, 0},
40   {&IMXRT_TMR1, 1,  12,  1, NULL, 0},
```

```
  {&IMXRT_TMR2, 0,  13,  1, &IOMUXC_QTIMER2_TIMER0_SELECT_INPUT, 1},
  {&IMXRT_TMR3, 2,  14,  1, &IOMUXC_QTIMER3_TIMER2_SELECT_INPUT, 1},
  {&IMXRT_TMR3, 3,  15,  1, &IOMUXC_QTIMER3_TIMER3_SELECT_INPUT, 1},
  {&IMXRT_TMR3, 1,  18,  1, &IOMUXC_QTIMER3_TIMER1_SELECT_INPUT, 0},
  {&IMXRT_TMR3, 0,  19,  1, &IOMUXC_QTIMER3_TIMER0_SELECT_INPUT, 1},
  // TODO: can 6 more be used with XBAR1 and GPR6 ?
};

#define NUM_TIMERS (sizeof(timerlist) / sizeof(timerinfo_t))

// gate interval interrupt deposits data here
volatile bool count_update = false;
volatile uint32_t count_output[NUM_TIMERS];

uint16_t read_count(unsigned int n) {
  static uint16_t prior[NUM_TIMERS];
  if (n >= NUM_TIMERS) return 0;
  uint16_t count = (timerlist[n].timer)->CH[timerlist[n].timerchannel].
   CNTR;
  uint16_t inc = count - prior[n];
  prior[n] = count;
  return inc;
}

void gate_timer() {
  static unsigned int count = 0;
  static uint32_t accum[NUM_TIMERS];

  for (unsigned int i=0; i < NUM_TIMERS; i++) {
    accum[i] += read_count(i);
  }
  if (++count >= GATE_ACCUM) {
    for (unsigned int i=0; i < NUM_TIMERS; i++) {
      count_output[i] = accum[i];
      accum[i] = 0;
    }
    count_update = true;
    count = 0;
  }
}

void setup() {

  Serial.begin(9600);
  // Header
  // Serial.println("- Teensy frequency counter -");
  // Serial.print(year()); Serial.print(" ");
  // Serial.print(month()); Serial.print(" ");
  // Serial.print(day()); Serial.print(" ");
  // Serial.println("Format: HH MM SS 001 002 003 004 005 006 007 008 009
   010");
  // Serial.println("Time elapsed since teensy is on");
  // Serial.println("--------------DATA--------------");

  // turn on clock to all quad timers
  CCM_CCGR6 |= CCM_CCGR6_QTIMER1(CCM_CCGR_ON) | CCM_CCGR6_QTIMER2(
   CCM_CCGR_ON)
    | CCM_CCGR6_QTIMER3(CCM_CCGR_ON) | CCM_CCGR6_QTIMER4(CCM_CCGR_ON);

  // configure all counting timers
```

```
98   for (unsigned int i=0; i < NUM_TIMERS; i++) {
99     IMXRT_TMR_t *timer = timerlist[i].timer;
100    int ch = timerlist[i].timerchannel;
101    timer->CH[ch].CTRL = 0;
102    timer->CH[ch].CNTR = 0;
103    timer->CH[ch].LOAD = 0;
104    timer->CH[ch].COMP1 = 65535;
105    timer->CH[ch].CMPLD1 = 65535;
106    timer->CH[ch].SCTRL = 0;
107    timer->CH[ch].CTRL = TMR_CTRL_CM(1) | TMR_CTRL_PCS(ch) |
     TMR_CTRL_LENGTH;
108    int pin = timerlist[i].pin;
109    *portConfigRegister(pin) = timerlist[i].pinconfig;
110    if (timerlist[i].inputselectreg) {
111      *timerlist[i].inputselectreg = timerlist[i].inputselectval;
112    }
113  }
114
115  // start gate interval timer
116  static IntervalTimer t;
117  t.begin(gate_timer, GATE_INTERVAL);
118 }
119
120 void loop() {
121   if (count_update) {
122     // Serial.print(year()+54);Serial.print(" ");
123     // Serial.print(month()+2);Serial.print(" ");
124     // Serial.print(day()+12);Serial.print(" ");
125     // Serial.print(hour());Serial.print(" ");
126     // Serial.print(minute());Serial.print(" ");
127     // Serial.print(second());Serial.print(" ");
128     for (unsigned int i=0; i < NUM_TIMERS; i++) {
129       Serial.printf("%8u ", count_output[i] * MULT_FACTOR);
130     }
131     Serial.println();
132     count_update = 0;
133   }
134 }
```

C.2 Python code used to read the data from the Teensy

```
1
2  import serial
3
4  serCon = False
5
6  try:
7      ser = serial.Serial('COM4', 9600)
8      serCon = True
9
10
11 except serial.serialutil.SerialException:
12     print("Warning: Arduino not connected")
13     pass
14
15 file_path = ("C:\\Users\\nordi\\Documents\\Cours_unif\\Memoire\\Teensy\\
       FreqCount\\ECH-RED-L11-4.txt")
16 #ser2 = serial.Serial('COM4', 9600)
```

```
17
18 if serCon:
19     try:
20         with open(file_path, 'w') as file:
21             while True:
22                 data = ser.readline().decode('utf-8')
23                 file.write(data)
24                 file.flush()
25                 print(data)
26     except Exception as e:
27         print("An error occured:", e)
28     finally:
29         ser.flush()
30         ser.close() #close the serial port
```

Bibliography

[1] Joshua D. Bishop et al. "Sensitivity enhancement in lateral flow assays: a systems perspective". In: *Royal society of chemistry* (2019). URL: https://pubs.rsc.org/en/content/articlehtml/2019/lc/c9lc00104b.

[2] Elif Burcu Bahadır and Mustafa Kemal Sezgintürk. "Lateral flow assays: Principles, designs and labels". In: *TrAC Trends in Analytical Chemistry* 82 (2016), pp. 286–306. ISSN: 0165-9936. DOI: https://doi.org/10.1016/j.trac.2016.06.006. URL: https://www.sciencedirect.com/science/article/pii/S0165993616300668.

[3] Bo Cao et al. "Development of magnetic sensor technologies for point-of-care testing: Fundamentals, methodologies and applications". In: *Sensors and Actuators A: Physical* (Sept. 2020). URL: https://www.sciencedirect.com/science/article/pii/S0924424719318539.

[4] Dorian VAN NIEUWENHOVE. "Planar inductors for detection of magnetic nanoparticles in a paper-based water quality monitoring system". Master thesis. UCLouvain, 2023.

[5] Van-Thuan Nguyen et al. "Recent advances in high-sensitivity detection methods for paper-based lateral-flow assay". In: *Biosensors and Bioelectronics* 152 (2020), p. 112015. ISSN: 0956-5663. DOI: https://doi.org/10.1016/j.bios.2020.112015. URL: https://www.sciencedirect.com/science/article/pii/S0956566320300129.

[6] Yanko Sheiretov. "Deep penetration magnetoquasistatic sensors". In: (May 19, 2005).

[7] Inga Ennen et al. "Giant Magnetoresistance: Basic Concepts, Microstructure, Magnetic Interactions and Applications". In: *Sensors* (June 17, 2016). URL: https://www.mdpi.com/1424-8220/16/6/904.

[8] Càndid Reig, María-Dolores Cubells-Beltrán, and Diego Ramírez Muñoz. "Magnetic Field Sensors Based on Giant Magnetoresistance (GMR) Technology: Applications in Electrical Current Sensing". In: *Sensors* 9.10 (2009), pp. 7919–7942. ISSN: 1424-8220. DOI: 10.3390/s91007919. URL: https://www.mdpi.com/1424-8220/9/10/7919.

[9] Shan X. Wang and Guanxiong Li. "Advances in Giant Magnetoresistance Biosensors With Magnetic Nanoparticle Tags: Review and Outlook". In: *IEEE Transactions on Magnetics* 44.7 (2008), pp. 1687–1702. DOI: 10.1109/TMAG.2008.920962.

[10] Wenlan Qiu et al. "Spin-Valve based magnetoresistive nanoparticle detector for applications in biosensing". In: *Sensors and Actuators A: Physical* (2017). URL: https://www.sciencedirect.com/science/article/pii/S0924424717306593.

[11] A. Chalastaras et al. "GMR multilayers on a new embossed surface". In: *IEEE Transactions on Magnetics* 40.4 (2004), pp. 2257–2259. DOI: 10.1109/TMAG.2004.830419.

[12] Ulrich Engelmann et al. "Key Contributors to Signal Generation in Frequency Mixing Magnetic Detection (FMMD): An In Silico Study". In: *Sensors* (Mar. 18, 2024). URL: https://www.mdpi.com/1424-8220/24/6/1945 (visited on 05/12/2024).

[13] Liang Tu et al. “Real-time measurement of Brownian relaxation of magnetic nanoparticles by a mixing-frequency method”. In: *Applied Physics Letters* (2011). URL: https://pubs.aip.org/aip/apl/article-abstract/98/21/213702/340316/Real-time-measurement-of-Brownian-relaxation-of?redirectedFrom=fulltext.

[14] Petr I. Nikitin, Petr M. Vetoshko, and Tatiana I. Ksenevich. “New type of biosensor based on magnetic nanoparticle detection”. In: (Apr. 2007). URL: https://www.sciencedirect.com/science/article/abs/pii/S0304885306025789 (visited on 05/12/2024).

[15] Amine Rabehi et al. “Magnetic Detection Structure for Lab-on-Chip Applications Based on the Frequency Mixing Technique”. In: *Sensors* 18.6 (2018). ISSN: 1424-8220. DOI: 10.3390/s18061747. URL: https://www.mdpi.com/1424-8220/18/6/1747.

[16] Alexey V. Orlov et al. “Rapid dry-reagent immunomagnetic biosensing platform based on volumetric detection of nanoparticles on 3D structures”. In: *Biosensors & Bioelectronics* 79 (May 15, 2016), pp. 423–429. ISSN: 1873-4235. DOI: 10.1016/j.bios.2015.12.049.

[17] José Luis Marqués-Fernández et al. “New Perspective on Planar Inductive Sensors: Radio-Frequency Refractometry for Highly Sensitive Quantification of Magnetic Nanoparticles”. In: *Sensors* 23.5 (Feb. 21, 2023), p. 2372. ISSN: 1424-8220. DOI: 10.3390/s23052372. URL: https://www.mdpi.com/1424-8220/23/5/2372 (visited on 01/04/2024).

[18] Julie Richardson et al. “A novel measuring system for the determination of paramagnetic particle labels for use in magneto-immunoassays”. In: (Dec. 2001), pp. 1127–1132. URL: https://www.sciencedirect.com/science/article/abs/pii/S095656630100241X (visited on 05/12/2024).

[19] Hans-Joachim Krause et al. “Magnetic particle detection by frequency mixing for immunoassay applications”. In: (Dec. 13, 2006). URL: https://www.sciencedirect.com/science/article/abs/pii/S0304885306025480 (visited on 05/12/2024).

[20] C. Marquina et al. “GMR sensors and magnetic nanoparticles for immuno-chromatographic assays”. In: (Oct. 2012), pp. 3495–3498. URL: https://www.sciencedirect.com/science/article/abs/pii/S0304885312001710 (visited on 05/12/2024).

[21] Marius Volmer et al. “On Detection of Magnetic Nanoparticles Using a Commercial GMR Sensor”. In: *2021 International Aegean Conference on Electrical Machines and Power Electronics (ACEMP) & 2021 International Conference on Optimization of Electrical and Electronic Equipment (OPTIM)* (May 11, 2021), pp. 1–6. URL: https://ieeexplore.ieee.org/document/9590055.

[22] L.K. Quynh et al. “Design Optimization of an Anisotropic Magnetoresistance Sensor for Detection of Magnetic Nanoparticles”. In: *Journal of Electronic Materials* (Nov. 29, 2018), pp. 997–1004. URL: https://link.springer.com/article/10.1007/s11664-018-6822-4 (visited on 05/12/2024).

[23] Amanda Moyano et al. “Carbon-Coated Superparamagnetic Nanoflowers for Biosensors Based on Lateral Flow Immunoassays”. In: *Biosensors* (July 22, 2020). URL: https://www.mdpi.com/2079-6374/10/8/80#app1-biosensors-10-00080.

[24] David Lago-Cachon et al. “Scanning Magneto-Inductive Sensor for Quantitative Assay of Prostate-Specific Antigen”. In: *IEEE* (June 5, 2017). ISSN: 1949-3088. DOI: 10.1109/LMAG.2017.2702108. URL: https://ieeexplore.ieee.org/document/7921588.

[25] J.J. Makiranta and J.O. Lekkala. "Modeling and Simulation of Magnetic Nanoparticle Sensor". In: *2005 IEEE Engineering in Medicine and Biology 27th Annual Conference.* 2005 IEEE Engineering in Medicine and Biology 27th Annual Conference. Shanghai, China: IEEE, 2005, pp. 1256–1259. ISBN: 978-0-7803-8741-6. DOI: 10.1109/IEMBS.2005.1616653. URL: http://ieeexplore.ieee.org/document/1616653/ (visited on 07/06/2023).

[26] *What is mutual induction.* https://www.electrical4u.com/?s=What+is+mutual+induction.

[27] Samuel J. Ling, William Moebs, and Jeff Sanny. "University Physics Volume 2". In: Houston, Texas, June 10, 2016. URL: https://openstax.org/books/university-physics-volume-2/pages/14-1-mutual-inductance.

[28] Sunderarajan Mohan et al. "Simple Accurate Expressions for Planar Spiral Inductances". In: *IEEE JOURNAL OF SOLID-STATE CIRCUITS* 34 (Oct. 1999). URL: http://smirc.stanford.edu/papers/JSSC99OCT-mohan.pdf.

[29] P. Pereira et al. "Rf integrated inductor modeling and its application to optimization-based design," Analog Integrated Circuits and Signal Processing". In: *Analog Integrated Circuits and Signal Processing* 73 (Aug. 7, 2011), pp. 47–55. URL: https://link.springer.com/article/10.1007/s10470-011-9682-x.

[30] K. Elangovan and Chandrika Sreekantan Anoop. "Simple and Efficient Relaxation-Oscillator-Based Digital Techniques for Resistive Sensors — Design and Performance Evaluation". In: *IEEE Transactions on Instrumentation and Measurement* 69.9 (2020), pp. 6070–6079. DOI: 10.1109/TIM.2020.2972048.

[31] Anwar Ulla Khan, Tarikul Islam, and Jamil Akhtar. "An Oscillator-Based Active Bridge Circuit for Interfacing Capacitive Sensors With Microcontroller Compatibility". In: *IEEE Transactions on Instrumentation and Measurement* 65.11 (2016), pp. 2560–2568. DOI: 10.1109/TIM.2016.2581519.

[32] V. Ferrari, D. Marioli, and A. Taroni. "Oscillator-based interface for measurand-plus-temperature readout from resistive bridge sensors". In: *IEEE Transactions on Instrumentation and Measurement* 49.3 (2000), pp. 585–590. DOI: 10.1109/19.850399.

[33] M.E.H Amrani et al. "Frequency counting interrogation techniques applied to gas sensor arrays". In: *Sensors and Actuators B: Chemical* (). URL: https://www.sciencedirect.com/science/article/pii/S0925400599001380 (visited on 05/18/2024).

[34] Javed S Gaggatur and Gaurab Banerjee. "Noise analysis in ring oscillator-based capacitance sensor interface". In: *2016 IEEE 59th International Midwest Symposium on Circuits and Systems (MWSCAS).* 2016, pp. 1–4. DOI: 10.1109/MWSCAS.2016.7870078.

[35] Hua Wang et al. "A frequency-shift CMOS magnetic biosensor array with single-bead sensitivity and no external magnet". In: *2009 IEEE International Solid-State Circuits Conference - Digest of Technical Papers.* 2009, 438–439, 439a. DOI: 10.1109/ISSCC.2009.4977496.

[36] Hua Wang, Constantine Sideris, and Ali Hajimiri. "A frequency-shift based CMOS magnetic biosensor with spatially uniform sensor transducer gain". In: *IEEE Custom Integrated Circuits Conference 2010.* 2010, pp. 1–4. DOI: 10.1109/CICC.2010.5617603.

[37] Sanju Thomas et al. "Particle Sensor Using Solidly Mounted Resonators". In: *IEEE Sensors Journal* 16.8 (2016), pp. 2282–2289. DOI: 10.1109/JSEN.2015.2512303.

[38] Staffan Johansson. “New frequency counting principle improves resolution”. In: *Proceedings of the 20th European Frequency and Time Forum*. 2006, pp. 139–146.

[39] Adel Sedra and Kenneth Smith. “Chapter 18 : Signal Generators and WaveformShaping Circuits”. In: *Microeletronics circuits seventh edition*, pp. 1379–1418. ISBN: 978-0-19-933913-6.

[40] Fritz Riehle. “Chapter 2 - Basics of Frequency Standards”. In: *Frequency Standards -Basics and application*, pp. 11–44. ISBN: 3-527-40230-6. URL: https://books.google.be/books?hl=en&lr=&id=q9AKk3smIJwC&oi=fnd&pg=PR7&dq=frequency+counting+for+oscillator+characterisation&ots=yEvQSIOpQj&sig=2Hpsj84EXr9c4eZrCDODWh redir_esc=y#v=onepage&q&f=false.

[41] Denis Flandre et al. *LELEC2532 Analog electronics - Oscillators*. 2016.

[42] Edwin H Colpitts. “Oscillation generator”. Pat. 214971. Apr. 12, 1927. URL: https://worldwide.espacenet.com/patent/search/family/022801117/publication/US1624537A?q=pn%3DUS1624537.

[43] Mehdi Azadmehr, Igor Paprotny, and Luca Marchetti. “100 Years of Colpitts Oscillators: Ontology Review of Common Oscillator Circuit Topologies”. In: (). DOI: 10.1109/MCAS.2020.3027334. URL: https://sci-hub.et-fine.com/10.1109/MCAS.2020.3027334 (visited on 01/28/2024).

[44] Tianshi Wang and Jaijeet Roychowdhury. “Rigorous Q Factor Formulation and Characterization for Nonlinear Oscillators”. In: (). URL: https://arxiv.org/pdf/1710.02015.pdf.

[45] Suhas Vishwasrao Shinde. “Review of Oscillator Phase Noise Models”. In: (Mar. 2014). URL: https://www.researchgate.net/profile/Suhas-Shinde/publication/287019272_Review_of_Oscillator_Phase_Noise_Models/links/5e07c4aaa6fdcc283745ee0c/Review-of-Oscillator-Phase-Noise-Models.pdf.

[46] David Bol. “LELEC2620 - Modeling and implementation of analog and mixed analog/digital circuits and systems on chip - Modeling and implementation Phase-Locked Loops (PLLs) David Bol April 20, 2018 ELEC2620”. Course lecture. Course lecture. 2024.

[47] D.B. Leeson. “A simple model of feedback oscillator noise spectrum”. In: *Proceedings of the IEEE* 54.2 (1966), pp. 329–330. DOI: 10.1109/PROC.1966.4682.

[48] Donhee Ham, William Andress, and David Ricketts. “PHASE NOISE IN OSCILLATORS”. In: (). URL: https://www.te.chiba-u.jp/lab/ken/Symp/Symp2004/PDF/1C3.PDF.

[49] A. Hajimiri and T.H. Lee. “A general theory of phase noise in electrical oscillators”. In: *IEEE Journal of Solid-State Circuits* 33.2 (1998), pp. 179–194. DOI: 10.1109/4.658619.

[50] Hua Wang, Ching-Chih Weng, and Ali Hajimiri. “Phase Noise and Fundamental Sensitivity of Oscillator-Based Reactance Sensors”. In: *IEEE Transactions on Microwave Theory and Techniques* 61.5 (2013), pp. 2215–2229. DOI: 10.1109/TMTT.2013.2256142.

[51] Amanda Moyano et al. “Magnetic Lateral Flow Immunoassay for Small Extracellular Vesicles Quantification: Application to Colorectal Cancer Biomarker Detection”. In: *Sensors* (May 28, 2021). URL: https://www.mdpi.com/1424-8220/21/11/3756.

[52] J.K. Clapp. “An Inductance-Capacitance Oscillator of Unusual Frequency Stability”. In: *Proceedings of the IRE* 36.3 (1948), pp. 356–358. DOI: 10.1109/JRPROC.1948.233920.

UNIVERSITÉ CATHOLIQUE DE LOUVAIN
École polytechnique de Louvain
Rue Archimède, 1 bte L6.11.01, 1348 Louvain-la-Neuve, Belgique | **www.uclouvain.be/epl**